



**HAL**  
open science

# Two-way coupling Eulerian numerical simulations of particle clouds settling in a quiescent fluid

Quentin Kriaa, Benjamin Favier, Michael Le Bars

► **To cite this version:**

Quentin Kriaa, Benjamin Favier, Michael Le Bars. Two-way coupling Eulerian numerical simulations of particle clouds settling in a quiescent fluid. *Physical Review Fluids*, 2023, 8 (7), pp.074302. 10.1103/PhysRevFluids.8.074302 . hal-04259023

**HAL Id: hal-04259023**

**<https://hal.science/hal-04259023>**

Submitted on 25 Oct 2023

**HAL** is a multi-disciplinary open access archive for the deposit and dissemination of scientific research documents, whether they are published or not. The documents may come from teaching and research institutions in France or abroad, or from public or private research centers.

L'archive ouverte pluridisciplinaire **HAL**, est destinée au dépôt et à la diffusion de documents scientifiques de niveau recherche, publiés ou non, émanant des établissements d'enseignement et de recherche français ou étrangers, des laboratoires publics ou privés.

# Two-way coupling Eulerian numerical simulations of particle clouds settling in a quiescent fluid

Quentin Kriaa,<sup>\*</sup> Benjamin Favier,<sup>†</sup> and Michael Le Bars<sup>‡</sup>  
*Aix Marseille Univ, CNRS, Centrale Marseille, IRPHE, Marseille, France*

(Dated: October 25, 2023)

To get a deeper understanding of our laboratory experiments [Kriaa *et al.*, Phys. Rev. Fluids 7(12) 124302 (2022)], we numerically model settling clouds produced by localised instantaneous releases of heavy particles in a quiescent fluid. By modelling particles as a field of mass concentration in an equilibrium Eulerian approach, our two-way coupling simulations recover our original experimental observation of a maximum growth rate for clouds laden with particles of finite Rouse number  $\mathcal{R} \approx 0.22$ . Consistent with the literature on buoyant vortex rings, our clouds verify the relation  $\alpha \propto \Gamma_\infty^{-2}$  between the clouds' growth rate  $\alpha$  and their eventually constant circulation  $\Gamma_\infty$ . As the Rouse number approaches  $\mathcal{R} \approx 0.22$ , the baroclinic forcing of the circulation reduces down to a minimum, thus optimising the cloud growth rate  $\alpha$ . This analysis highlights the role of the mean flow in the enhanced entrainment of ambient fluid by negatively buoyant clouds. Our results also validate, on the basis of direct comparison with experimental results, the use of a one-fluid two-way coupling numerical model to simulate particle clouds in the limit of weak particle inertia.

## I. INTRODUCTION

The present study follows up on a series of 514 systematic laboratory experiments presented in Kriaa *et al.* [1] which focus on the evolution of instantaneously-released particle-laden clouds settling from rest in initially quiescent water, under the sole action of their buoyancy. By varying the size of particles yet keeping an identical buoyancy for all clouds, the latter proved to grow linearly in depth with a growth rate  $\alpha$  that reaches a maximum for a finite particle inertia  $\mathcal{R} \simeq 0.3 \pm 0.1$ , where the Rouse number  $\mathcal{R} = w_s/U_{\text{ref}}$  is the ratio of the terminal velocity of an isolated particle  $w_s$  over the reference fall velocity  $U_{\text{ref}}$  of the cloud due to the sole action of its buoyancy. This new observation was unexpected because the theory of turbulent thermals [2], commonly used to model such clouds, predicts that all clouds should grow similarly as a salt-water cloud of identical buoyancy. Yet, our measurements revealed that the particle inertia can increase the growth rate by up to 75%. Our experiments did not enable us to answer some remaining questions: Through what mechanism do particle clouds entrain more than salt-water clouds of identical buoyancy? In particular, does the particle inertia alter the mean flow around the cloud or does it modulate the intensity of the turbulence that develops inside the cloud? The aim of the present study is to gain understanding on these questions thanks to complementary Direct Numerical Simulations (DNS). The numerical approach to be adopted should capture the macroscopic physics of particle clouds as observed in our experiments, yet with the minimum ingredients to keep a low numerical cost, with a motivation to later apply the method to a planetary-scale multiphase flow called 'iron snow' [3].

When the size of particles, their volume fraction and the particle-to-fluid density anomaly are low, the fluid governs the motion of particles whose feedback on the flow is negligible, a situation called *one-way coupling* [4]. Many studies have considered the one-way coupling between particles and fluid motions (e.g. [5–9]) and evidenced that inertia is a source of non-uniformities in the field of particle concentration [10]: despite the incompressibility of the fluid phase, inertia allows the disperse phase to be compressible. M. R. Maxey [10] showed that very small particles behave as passive tracers due to their low inertia; conversely, large particles are insensitive to local modifications of the flow due to their large response time (see also [7, 11]). Due to this low-pass 'inertial filtering' of timescales, dense particles of intermediate size partly decouple from fluid motions. For some finite inertia they have been observed to optimally couple with the surrounding flow and concentrate in some specific regions. This phenomenon of 'preferential concentration' ([10], see also [7, 9, 12–14]) leads to the accumulation of small particles in regions of large strain rate or equivalently of low vorticity [10], possibly due to centrifuging of particles outside of vortices [5, 9], while larger dense particles rather concentrate in regions of vanishing fluid acceleration [8, 15].

With the addition of gravity, another heterogeneity originates from the tendency of heavy particles to fall on the side of downward velocity of eddies [16], which can be grasped by simple advective arguments even in laminar flows (e.g. [17]). This phenomenon of 'fast tracking' or 'preferential sweeping' is also optimum for a finite particle inertia

---

<sup>\*</sup> Corresponding author: quentin.kriaa@univ-amu.fr

<sup>†</sup> benjamin.favier@cnrs.fr

<sup>‡</sup> michael.le-bars@univ-amu.fr

[16]; it has been observed in 2D periodic laminar vortices [18] and in turbulent flows (e.g., [6, 9, 19–21]). Additionally, due to their inertia, falling particles lag behind fluid motions so their trajectories are biased in the direction of gravity. As particles cross upwelling and downwelling regions, they spend more time in upwelling regions, increasing their sensitivity to velocity variations in these upwellings. This ‘loitering’ [17] is a third example of preferential sampling of the flow.

All these phenomena of preferential sampling determine the distribution of particles in time and space. This observation is paramount if the flow is altered by the feedback of particles on the fluid, a situation referred to as *two-way coupling* [4]. Inclusion of this feedback in numerical simulations has proved to be essential as it further modifies the structure of particle-laden flows even in well-controlled idealised isotropic turbulent flows [19–22], especially in the presence of gravity which breaks the flow isotropy. As an example, experiments [12] and simulations [21, 22] have shown that the non-linear modification of the settling velocity due to preferential concentration and preferential sweeping is further favoured by two-way coupling since clusters of particles drag fluid with them as they sweep downward, producing downward acceleration of the fluid which enhances the fluid velocity and therefore the particle settling velocity. Most importantly, even in the presence of low mass loadings, the feedback of particles on the fluid is essential if the flow is driven by the particles themselves, e.g. in downdrafts [23], turbidity currents [24, 25], and presumably iron snow [3]. The present work fits in this framework: in our experiments [1] particles were released from rest in quiescent water, hence all fluid motions resulted from the drag exerted by particles on water during their fall.

Thus, in this study we adopt an equilibrium Eulerian approach [4] to model our settling particle clouds at reasonably low numerical cost, while still accounting for the two essential ingredients of (i) the feedback of particles on the fluid through a drag term which forces the flow, and (ii) a differential motion between water and settling particles through a gravitational drift, a formalism already used in the literature to model particle-laden flows [26–30]. The latter effect is quantified by a Rouse number which is about  $\mathcal{R} = 0.3$  for the optimum growth rate in experiments, and which lies below unity for most of our clouds. Our experiments therefore fit in the range of validity of the equilibrium Eulerian model, as pointed out by Boffetta *et al.* [27]. Note however that we extend our analysis up to  $\mathcal{R} \simeq 3$  as in our experiments. Boffetta *et al.* [27] showed that such particles have so much inertia that they undergo the ‘sling effect’ i.e. particles tend to converge and thereby form caustics, so that the continuum modelling of particle motions through a unique velocity field locally breaks down. Yet, our results using the equilibrium Eulerian formalism up to  $\mathcal{R} \simeq 3$  show good agreement with our experiments, supporting the fact that if the sling effect plays any part in experiments, it still has no strong statistical signature on the macroscopic quantities we measured in experiments and reproduce numerically here.

The paper is organised as follows. Section II introduces the equations of motion to model particles as a field of mass concentration verifying an advection-diffusion equation and forcing the flow through a drag term. Section III presents the numerical setup of the three-dimensional numerical simulations. Then, section IV presents the two main regimes of cloud settling; it notably evidences the same maximum of the cloud growth rate  $\alpha$  as observed in our experiments [1]. Section V is devoted to the analysis of this effect, showing that particles with a Rouse number close to the optimum impose a weaker baroclinic forcing of the clouds’ circulation, resulting in an enhanced growth rate according to the theory of buoyant vortex rings. Further discussion and concluding remarks are presented in section VI. Appendix A provides details on the robustness of the numerical simulations, and appendix B gives numerical results for particle clouds of larger Reynolds number than those presented in the core of this study.

## II. EQUATIONS OF MOTION

If a particle has finite inertia and is not neutrally buoyant, it moves with a velocity  $\mathbf{v}_p$  which is different from that of the fluid  $\mathbf{v}$  in its vicinity, and the particle acceleration verifies its own momentum equation. This momentum equation for a small spherical particle was established in 1983 by [31] under the assumptions that the particle of radius  $r_p$  is much smaller than the characteristic macroscopic length scale  $L$  of the flow, that the particle Reynolds number based on the slip velocity of the particle is much lower than unity (so the disturbance flow due to the particle can be considered a Stokes flow), and that the diffusive timescale  $r_p^2/\nu$  is much lower than the advective timescale  $L/U_0$  ( $\nu$  being the kinematic viscosity of the fluid and  $U_0$  a characteristic velocity scale of the flow). With these assumptions, the leading terms boil down to the particle acceleration, its buoyancy and the Stokes drag exerted by the fluid. Furthermore, in the equilibrium Eulerian formalism, assuming that all particles have very small inertia (limit of vanishingly small Stokes numbers), the particle acceleration can be neglected [4] so that the particle velocity is solely prescribed by the balance between buoyancy and drag [9, 32]. This balance yields

$$\mathbf{v}_p = \mathbf{v} + w_s \mathbf{e}_z, \quad (1)$$

as derived in [33], where  $\mathbf{v}$  is the fluid velocity,  $\mathbf{v}_p$  is the particle velocity,  $w_s$  is the terminal velocity of the particle in quiescent fluid and  $\mathbf{e}_z = \mathbf{g}/\|\mathbf{g}\|$  is aligned with the gravity field  $\mathbf{g}$ . In the present study we use this approximation to

the momentum equation even for particles with non negligible inertia, and try to assess the accuracy of this approach. To keep a moderate numerical cost, as in previous studies of particle-laden flows [26–30, 34, 35] we model particles as a continuum with a field of concentration  $\mathcal{C}$  (mass of particles per unit volume) that is advected at the velocity  $\mathbf{v}_p$ , hence, mass conservation reads

$$\partial_t \mathcal{C} + \mathbf{v}_p \cdot \nabla \mathcal{C} = 0. \quad (2)$$

In practice, such modelling neglects particle dispersion at the particle scale. In fact, even in dilute suspensions for which collisions are negligible, and even in the absence of Brownian motions, particles induce long-range perturbations, particle-wake interactions and collective-settling effects in the fluid depending on their particulate Reynolds number (e.g. [36–39]). These perturbations lead to a dispersion which has been analysed analytically [40], numerically [41] and experimentally [42–46], and which can be approximated by a diffusive process. Together with other ingredients such as concentration gradients and shear [47], these effects are referred to as a hydrodynamic diffusion [48]. They are often approximated at a macroscopic level by a term of diffusion in the mass conservation above [33, 44, 46, 49]. In addition, including a diffusive term in the mass conservation equation is necessary to prevent the formation of caustics in the field of particle concentration, which would lead to numerical instabilities in the current Eulerian framework [34]. By introducing the effective particle diffusivity  $\kappa_p$ , and using equation (1), the new equation of mass conservation reads

$$\partial_t \mathcal{C} + \mathbf{v} \cdot \nabla \mathcal{C} = \kappa_p \nabla^2 \mathcal{C} - w_s \frac{\partial \mathcal{C}}{\partial z}, \quad (3)$$

where the last term accounts for the gravitational drift of particles.

Fluid motions are constrained by the condition of incompressibility

$$\nabla \cdot \mathbf{v} = 0, \quad (4)$$

which also prescribes the incompressibility of the field of concentration using equation (1). The fluid velocity  $\mathbf{v}$  verifies the Navier-Stokes equation for a Newtonian fluid

$$\frac{\partial \mathbf{v}}{\partial t} + \mathbf{v} \cdot \nabla \mathbf{v} = -\frac{1}{\rho_f} \nabla p + \nu \nabla^2 \mathbf{v} + \frac{1}{\rho_f} \mathbf{f}_{\text{drag}}, \quad (5)$$

where  $\rho_f$  is the fluid density,  $p$  is the pressure field including the hydrostatic contribution,  $\nu$  is the constant fluid kinematic viscosity, and  $\mathbf{f}_{\text{drag}}$  is the average drag force exerted by particles on the fluid per unit volume. This drag term in equation (5) describes how particles force the flow: the field of concentration and the fluid are now two-way coupled. The present model is derived for supposedly spherical particles of vanishingly small Reynolds number, hence they fall in the Stokes regime with a settling velocity

$$w_s^{\text{Stokes}} = \frac{2gr_p^2(\rho_p - \rho_f)}{9\nu\rho_f}, \quad (6)$$

with  $\rho_p$  the density of a spherical particle of radius  $r_p$ . Then, using equation (1), the Stokes drag exerted by the fluid on a particle reads  $-6\pi\rho_f\nu r_p w_s^{\text{Stokes}} \mathbf{e}_z$ . Summation on all the particles in the unit volume requires to multiply this individual acceleration by the number of particles per unit volume i.e.  $3\mathcal{C}/4\pi r_p^3 \rho_p$ . Using Newton's third law, the drag force reads

$$\mathbf{f}_{\text{drag}} = \mathcal{C} \frac{\rho_p - \rho_f}{\rho_p} \mathbf{g}. \quad (7)$$

The previous equations are non-dimensionalised using the diameter of the release cylinder  $D_{\text{cyl}}$  and the characteristic velocity that clouds can build up when accelerating from rest which is

$$U_{\text{ref}} = \sqrt{g \left(1 - \frac{\rho_f}{\rho_0}\right) D_{\text{cyl}}}, \quad (8)$$

where  $\rho_0 = \rho_f + (1 - \rho_f/\rho_p)m_0/(4\pi D_{\text{cyl}}^3/3)$  is the typical initial effective density of particle clouds (see Ref. [1] for details). Time  $t$ , pressure  $p$  and concentration  $\mathcal{C}$  are respectively non-dimensionalised by the advective timescale

$D_{\text{cyl}}/U_{\text{ref}}$ , the characteristic dynamic pressure  $\rho_f U_{\text{ref}}^2$ , and the fluid density  $\rho_f$ . With the dimensionless variables, equation (4) is unmodified while mass conservation now reads

$$\partial_t \mathcal{C} + \mathbf{v} \cdot \nabla \mathcal{C} = \frac{1}{Pe} \nabla^2 \mathcal{C} - \underbrace{\mathcal{R} \frac{\partial \mathcal{C}}{\partial z}}_{\text{gravitational drift}}, \quad (9)$$

where  $Pe = U_{\text{ref}} D_{\text{cyl}} / \kappa_p$  is the Péclet number, and  $\mathcal{R} = w_s / U_{\text{ref}}$  is the Rouse number which characterises the gravitational drift of particles. When  $\mathcal{R} \ll 1$  particles hardly drift with respect to the fluid and tend to follow fluid motions, whereas particles having  $\mathcal{R} \gg 1$  largely decouple by vertical settling so their trajectories largely differ from those of fluid particles in their vicinity. Using equation (7), similar non-dimensionalisation of equation (5) leads to

$$\frac{\partial \mathbf{v}}{\partial t} + \mathbf{v} \cdot \nabla \mathbf{v} = -\nabla p + \frac{1}{Re} \nabla^2 \mathbf{v} + \underbrace{Ri \mathcal{C} \mathbf{e}_z}_{\text{drag term}}, \quad (10)$$

where  $Re = U_{\text{ref}} D_{\text{cyl}} / \nu$  is the Reynolds number and  $Ri = g D_{\text{cyl}} (1 - \rho_f / \rho_p) / U_{\text{ref}}^2$  is the Richardson number which boils down to a ratio of density contrasts  $Ri = (1 - \rho_f / \rho_p) / (1 - \rho_f / \rho_0)$  for our specific choice of  $U_{\text{ref}}$  used to non-dimensionalise the equations.

### III. NUMERICAL SETUP

The numerical setup aims at reproducing the experimental conditions for the generation of our particle clouds [1], released with no initial velocity from the top centre of a tank of still water. Every particle cloud is composed of  $m_0 = 1g$  of spherical glass beads with a mean radius  $r_p$  chosen in the range  $5\mu\text{m}-1\text{mm}$ , as well as some water, sometimes dyed with rhodamine. All this material is initially contained in a cylinder of diameter  $D_{\text{cyl}}$  partially immersed in water and sealed by a latex membrane. When an experiment starts, the membrane is ruptured by a needle, it quickly retracts and lets particles settle from rest in the tank with the dyed fluid. Visualisations are performed in a vertical green laser sheet with two cameras: the one with a green filter records the motion of particles only, while the camera with an orange filter records only motions of turbulent eddies dyed with rhodamine, see figure 1a for an illustration. Some reference clouds without particle inertia contained an identical mass excess  $m_0 = 1g$  of salt water and were generated in the same way. Their dynamics is characterised by a Rouse number  $\mathcal{R} = 0$ . Experiments were performed in a tank of depth 1m with horizontal square cross section of  $42 \times 42\text{cm}^2$  surface area; the side walls of the tank were considered far enough from particle clouds to have negligible influence on the settling of particles. In the present simulations, the computational domain represents a cube of volume  $1\text{m}^3$  with side length  $L_{\text{domain}} = 31.25 D_{\text{cyl}}$ . Figure 1b shows a numerical analog of our experimental clouds in a simulation having  $\mathcal{R} = 0.221$  at time  $t = 34$ .

To model the instantaneous release of particles from the cylinder, the field of concentration is initialised in a narrow cylindrical region of diameter  $D_{\text{cyl}}$ , horizontally centred and localised at distance  $1.5 D_{\text{cyl}}$  below the top of the computational domain. In experiments particles rested at the bottom of the cylinder on the latex membrane as a very thin layer of height  $H_{\text{compact}}$ . To smooth the initial concentration gradients required to model the initial layer, the field of concentration is initialised in a cylindrical region of height  $10 H_{\text{compact}}$ , and the lateral and vertical edges of this cylindrical region are smoothed by a hyperbolic tangent with typical length scale  $H_{\text{compact}}$ . The factor 10 on the initial height of the pile of particles is expected to have negligible influence: indeed, our experiments showed that varying the height of the pile of particles from  $H_{\text{compact}}$  to  $40 H_{\text{compact}}$  had negligible impact on the dynamics we aim to model here (see [1] for further details). To compensate for the errors introduced the hyperbolic tangent smoothing, the exact mass of particles is enforced (in dimensional form,  $m_0 = 1g$ ) by an appropriate rescaling. The uniform fluid is initially motionless, save for a cylindrical envelope around particles at time  $t = 0$  in which the velocity field is perturbed by a random uniform infinitesimal noise.

A passive tracer is implemented to mimic rhodamine in simulations. This tracer is initialised exactly like the concentration  $\mathcal{C}$  and satisfies equation (9) with its own Rouse number  $\mathcal{R} = 0$  so it does not drift vertically as particles do. Importantly, unlike the field of particle concentration  $\mathcal{C}$ , the passive tracer does not force any flow (it is absent of equation (10)).

On all walls, the velocity field satisfies no slip boundary conditions, while the concentration  $\mathcal{C}$  and the passive tracer satisfy no-flux Neumann boundary conditions.

Equations (4), (9) and (10) are integrated in three dimensions with the solver Basilisk [50] that is second-order accurate in space and time, using a time-splitting pressure-correction discretisation of the Navier-Stokes equation (10). The second-order advection scheme of Bell-Colella-Glaz [51] is used for equation (10) and for the two advection

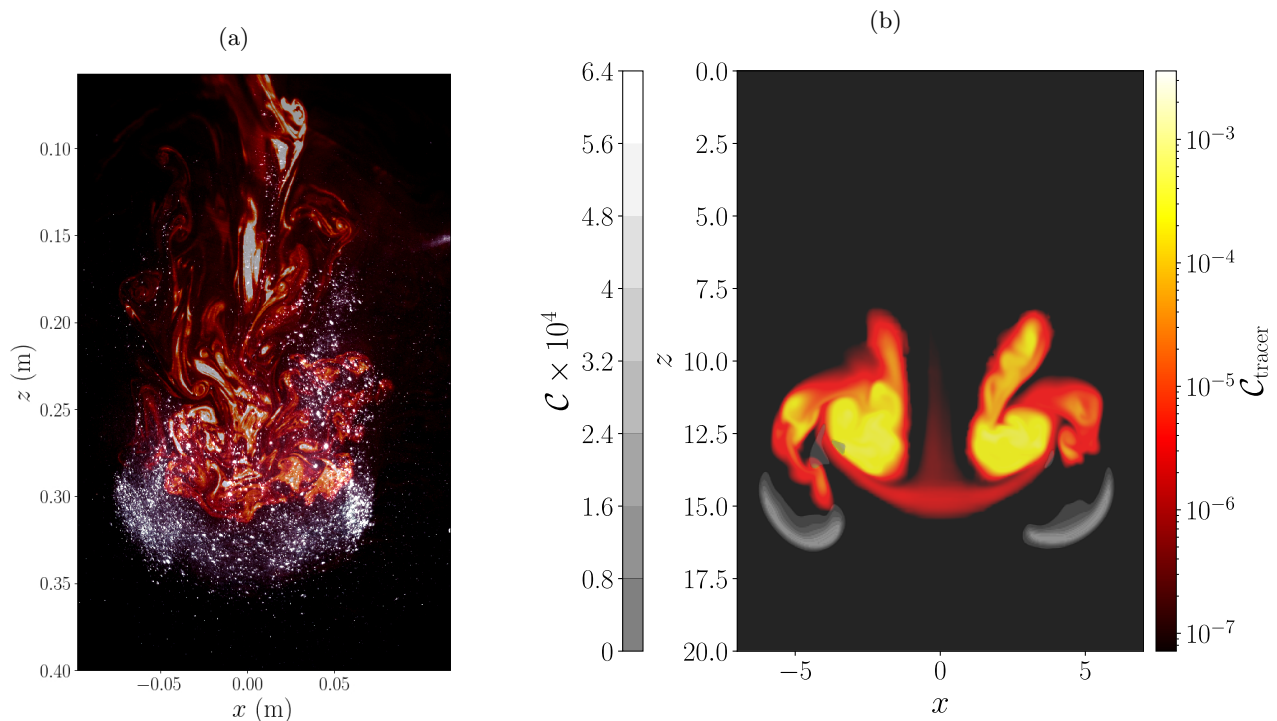


FIG. 1: (a) Visualisation of an experimental particle cloud in a vertical laser sheet with particles in grey (set of polydisperse particles of Rouse number  $\mathcal{R} = 0.308 \pm 0.080$ ) and dye (rhodamine) in orange. (b) Numerical analog in the plane  $y = 0$  of the previous photograph with a grey field of concentration  $\mathcal{C}$  modelling particles and an orange tracer concentration  $\mathcal{C}_{\text{tracer}}$  modelling dye (cloud of Reynolds number  $Re = 1183$  as in the experiment (a), with a fixed Rouse number  $\mathcal{R} = 0.221$ ). The larger vertical spread of particles in (a) compared to (b) is due to the polydispersity of the former, whereas simulations are performed for monodisperse particle clouds (see Kriaa *et al.* [1] for further details).

terms in equation (9). The concentration gradient  $\partial\mathcal{C}/\partial z$  is computed with the generalised minmod slope limiter [52] to reduce spurious oscillations due to sharp concentration gradients at initial times, with negligible impact on our numerical measurements (see appendix A). Due to the large scale separation between the domain size and the initial cloud size ( $L_{\text{domain}} = 31.25D_{\text{cyl}}$ ), an adaptive mesh refinement is adopted. This octree mesh is made of hierarchically organised cubic cells, each refinement of a cell corresponding to a division of this cell in 8 identical cubes. This refinement is based on local values of the concentration  $\mathcal{C}$  and on the local viscous dissipation, see an illustration in figure 2a. The smallest mesh cell has a size fixed to  $L_{\text{domain}}/1024$  while the largest mesh cell has a size  $L_{\text{domain}}/128$ .

Our main focus is to analyse the influence of gravitational settling on the evolution of particle clouds by varying the Rouse number from  $\mathcal{R} = 0$  to  $\mathcal{R} = 3.03$ . Consequently, with a fixed density  $\rho_p = 2500 \text{ kg/m}^3$  for all particles, the Richardson number  $Ri = 138$  does not vary between simulations, and the same conclusion holds for  $Re$  and  $Pe$ . These last two numbers are equal because we assume  $\nu = \kappa_p$  as a first approximation. The value  $Re = 454$  is chosen by following this conservative estimate: if the particle clouds were highly inertial and if their turbulence was homogeneous and isotropic with a fully-developed energy cascade from the integral cloud scale of order  $\sim 3D_{\text{cyl}}$  to the Kolmogorov scale, then the latter would have a size  $3D_{\text{cyl}}Re^{-3/4}$ . By prescribing that this smallest length scale should have a size  $L_{\text{domain}}/1024$ , this prescribes the value of  $Re = (L_{\text{domain}}/3072D_{\text{cyl}})^{-4/3} = 454$ . This calculation is conservative as no flow structure reaches such a small length scale in our simulations. In fact, the transient cloud formation does not permit the development of an energy cascade down to the Kolmogorov scale. Instead, the clouds we model are close to laminar, with a predominating coherent structure of size  $\sim 3D_{\text{cyl}}$ , confirming that all length scales are appropriately resolved. An example of the fields obtained is shown in figure 2b. For completeness, additional simulations at  $Re = 1183$  (which is the Reynolds number of particle clouds in our experiments [1]) are presented in appendix B which show similar results as those presented in the core of the present analysis.

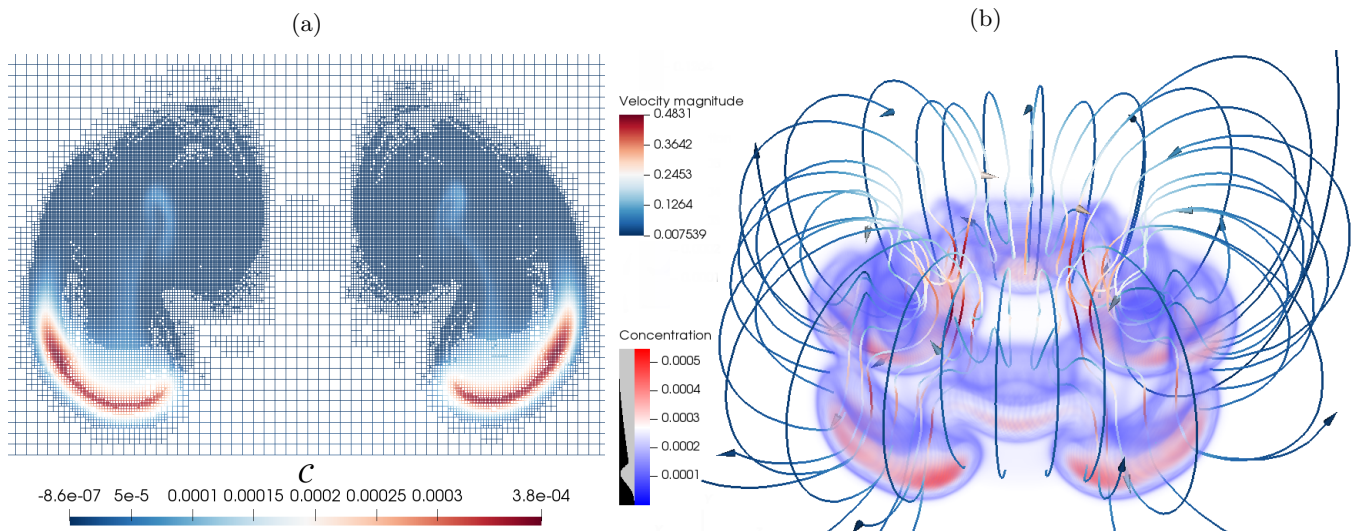


FIG. 2: (a) Adaptive mesh refinement on the field of concentration  $C$  for  $\mathcal{R} = 0.221$  in the plane  $y = 0$  at time  $t = 35$ . (b) Bird's eye view of the 3D structure of  $C(x, y, z, t = 33.75)$  for  $\mathcal{R} = 0.221$  in blue-red colours (colorbar and opacity in the bottom left-hand corner). Streamlines show the toroidal velocity field, with blue-red colours for the velocity magnitude  $\|\mathbf{v}\|$  (colorbar in the top left-hand corner).

## IV. REGIMES OF CLOUD SETTLING

### A. Overview

Figure 3 shows snapshots as well as an average image of the field of concentration  $C(x, y = 0, z, t)$  in a vertical cross section of the computational domain. They faithfully account for all the qualitative morphological features observed in our experiments (see figure 4 in Kriaa *et al.* [1]). Particle clouds initially grow as they propagate downward. For the lowest Rouse numbers this regime of growth and dilution lasts over the entire fall of the cloud. For intermediate Rouse numbers, this regime is more prominent (see figure 3c), yet this growth gradually vanishes and stops (see in particular average images in figures 3d, 3e). This transition is due the field of concentration separating from eddies, which is why the field of concentration deforms less and less, and settles more and more vertically.

The cloud evolution can be quantified by tracking the vertical position  $z_f(t)$  of its front, defined as the lowermost position of the iso-contour of concentration  $C(x, y, z, t) = 10^{-8}$  (this low value ensures that measurements are independent of the specific threshold), and by tracking the vertical position  $z(t)$  of the centre of mass, defined as the weighted average of the vertical coordinate  $z$  in the whole computational domain as  $z(t) = \int zC / \int C$ . Figure 4 shows the evolution of these two positions in time; for all figures we use dashed lines if  $\mathcal{R} > 0.221$  and solid lines otherwise, with grey shades diverging from the thick darkest line of  $\mathcal{R} = 0.221$ . For low Rouse numbers ( $\mathcal{R} < 1$ ), after a short phase of acceleration, the positions  $z_f(t)$  and  $z(t)$  evidence a concave evolution revealing the cloud deceleration. For intermediate Rouse numbers, a smooth transition occurs that leads to a regime of constant settling velocity when particles separate from fluid motions and settle in quiescent liquid. For the largest Rouse numbers ( $\mathcal{R} > 1$ ), clouds almost immediately transition from the regime of acceleration to the regime of constant settling velocity. The literature [1, 53–55] distinguishes between the first regime of turbulent thermal, or equivalently of buoyant vortex ring, and the second regime of swarm. All these observations are consistent with our experimental observations, which were obtained by tracking the front of the light intensity reflected by the glass spheres in time, which is analogous to  $z_f$  here. In the next sections, the two regimes of buoyant vortex ring and swarm are described separately.

### B. Buoyant vortex ring regime (*aka thermal regime*)

Due to the lower cloud Reynolds number in numerical simulations than in experiments (see appendix B for results at higher Reynolds number), numerical results evidence clear buoyant vortex rings whose toroidal structure is less apparent in our more turbulent thermals in the laboratory. Yet, several studies have shown that turbulent thermals

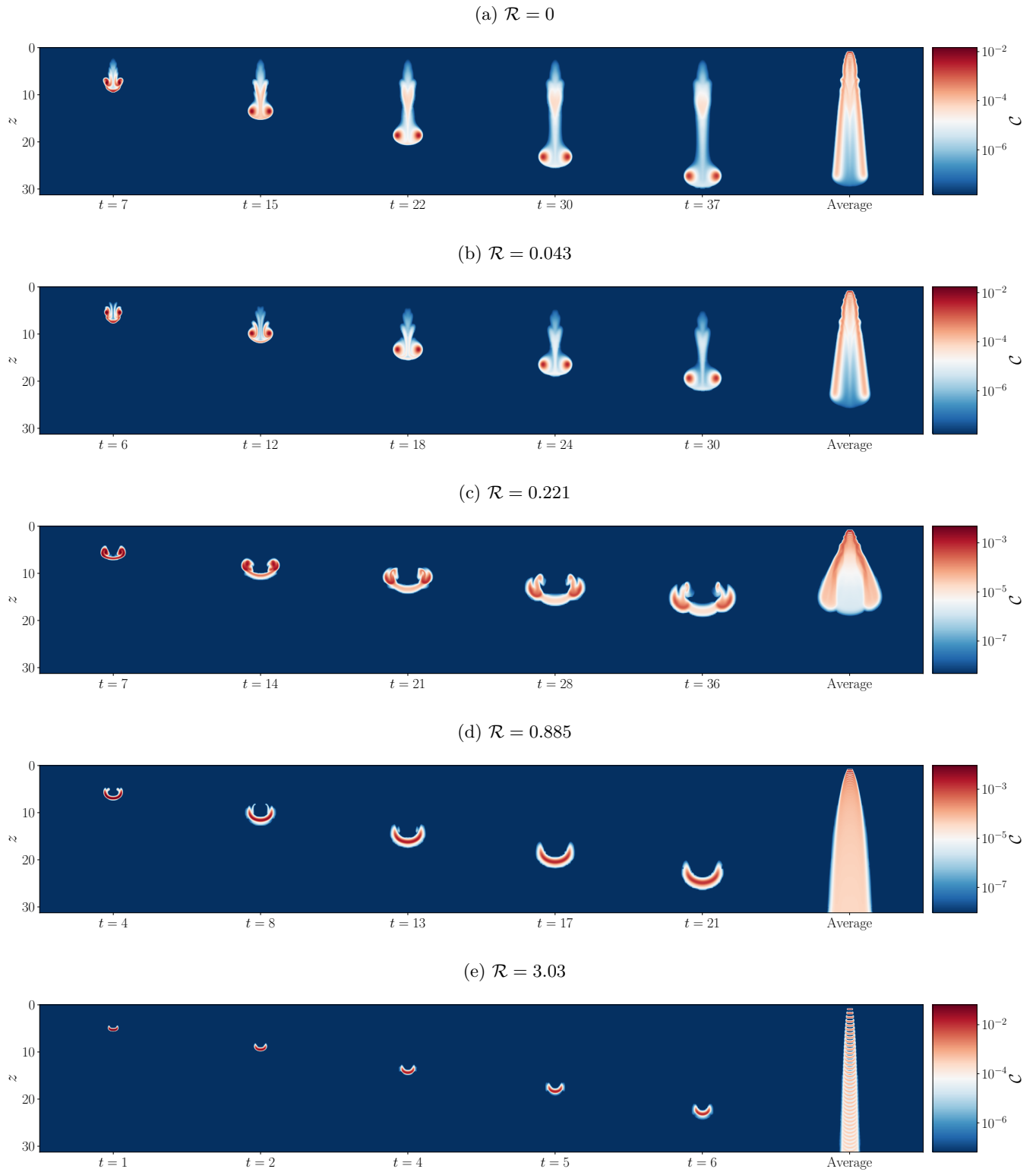


FIG. 3: Each row shows snapshots of the field of concentration  $\mathcal{C}(t, x, z)$  in the plane  $y = 0$  for a different Rouse number, as well as the average of 40 snapshots taken with a constant timestep  $\Delta t = 1$  over the fall.

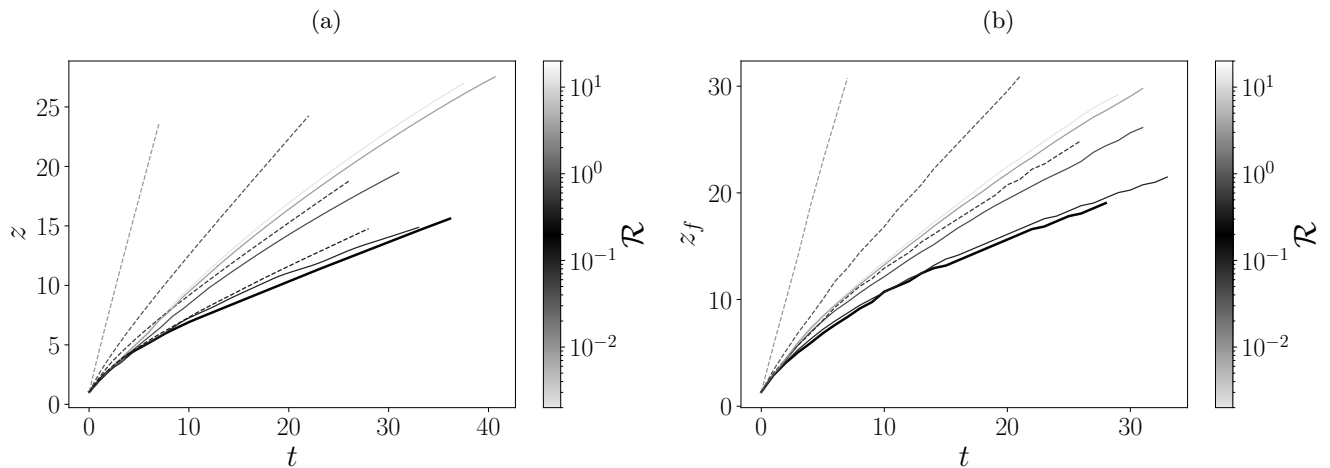


FIG. 4: For several Rouse numbers, evolution in time of the vertical position of (a) the centre of mass of particles, and of (b) the cloud front. Lines are dashed if  $\mathcal{R} > 0.221$  and solid otherwise.

(i.e. instantaneous releases of a finite volume of buoyant fluid with no initial momentum) are formed like buoyant vortex rings [56, 57], and have a very similar structure [58–61] and dynamics [62, 63], to such an extent that thermals have been considered as buoyant vortex rings whose circulation is fully determined by their buoyancy [64, 65]. Consistently, turbulent thermals at the cap of starting plumes [66], immiscible thermals [63] and settling particle clouds [67–69] have all been successfully modelled as vortex rings. In fact, different models of turbulent thermals (for example, references [2, 70]) and models of buoyant vortex rings [61, 62, 71] lead to the same scalings after the transient formation of these structures. Given the morphology of clouds in figure 3, we present the essential equations governing the evolution of buoyant vortex rings, which will prove enlightening to analyse the clouds growth.

When buoyant particles start settling, the cloud initially rolls up as a buoyant vortex ring. After a transient, one observes that vorticity concentrates inside a toroidal core. It is often assumed, and appropriate in our simulations as we shall see, that the vortex ring is sufficiently thin-cored to guarantee the absence of any buoyant material along the vortex centreline (axis of symmetry of the vortex ring, parallel to  $\mathbf{e}_z$  and passing through the centre of symmetry of the torus), and that no vorticity diffuses through this line, leading to the conclusion that the circulation  $\Gamma$  of the vortex ring remains constant after the short transient of spin-up (see equation 4 in reference [61]), as verified in numerical simulations for a cloud Reynolds number of 630 and 6300 [61]. Consequently, the initial spin-up of the vortex is paramount because it sets the ultimately constant value of the circulation which plays a key role in determining the cloud growth rate.

The impulse of a thin-cored vortex ring of radius  $R$  under the Boussinesq approximation reads  $\pi\rho_f\Gamma R^2$  [61, 62]. This impulse varies in time due to buoyancy which is the sole external force, hence we have

$$\frac{d}{dt} [\pi\rho_f\Gamma R^2] = m_0g, \quad (11)$$

from which it is clear that in the absence of buoyancy, the impulse would be constant hence the vortex ring would keep a constant radius, as verified in the literature [57, 72] for vortex rings of Reynolds number up to  $10^4$  [72]. Assuming a constant circulation, the previous equation simplifies to

$$R(t)^2 - R^2(t=0) = \frac{m_0g}{\pi\rho_f\Gamma} t. \quad (12)$$

To verify this scaling, the cloud radius is measured in numerical simulations with the quantity  $\sigma_h$ , which is the horizontal standard deviation of the particles' spatial distribution with respect to the cloud centre of mass

$$\sigma_h(t) = \sqrt{\frac{\int \mathcal{C}(x', y', z', t)(x'^2 + y'^2)}{\int \mathcal{C}(x', y', z', t)}}, \quad (13)$$

where the origin of coordinates  $(x', y', z')$  corresponds to the cloud centre of mass, and integrals are computed in the whole computational domain. From this definition, the scaling (12) is verified in figure 5: aside from slight oscillations,

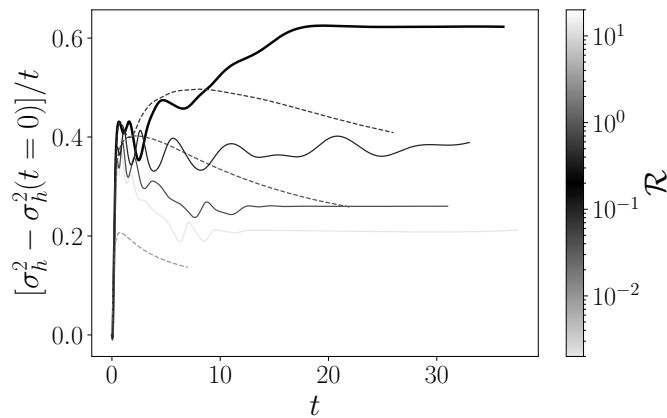


FIG. 5: Time evolution of the increment of square radius compensated with time  $[\sigma_h^2(t) - \sigma_h^2(t=0)]/t$ , measured in simulations for several Rouse numbers. Lines are dashed if  $\mathcal{R} > 0.221$  and solid otherwise.

clouds of low Rouse number ( $\mathcal{R} \leq 0.221$ ) eventually grow as  $\sigma_h \sim t^{1/2}$  as evidenced by the plateau of the compensated quantity  $[\sigma_h^2 - \sigma_h^2(t=0)]/t$ . Conversely, clouds with large Rouse numbers ( $\mathcal{R} > 0.221$ ) grow slower than  $\sigma_h \sim t^{1/2}$  so the quantity  $[\sigma_h^2 - \sigma_h^2(t=0)]/t$  eventually decreases in time, meaning that these clouds do not follow the scaling (12). Note that according to equation (12), the plateaus in figure 5 are inversely proportional to the circulation  $\Gamma$ , suggesting the existence of a minimum of circulation for intermediate Rouse numbers close to  $\mathcal{R} = 0.221$ ; this observation will receive considerable attention in section V.

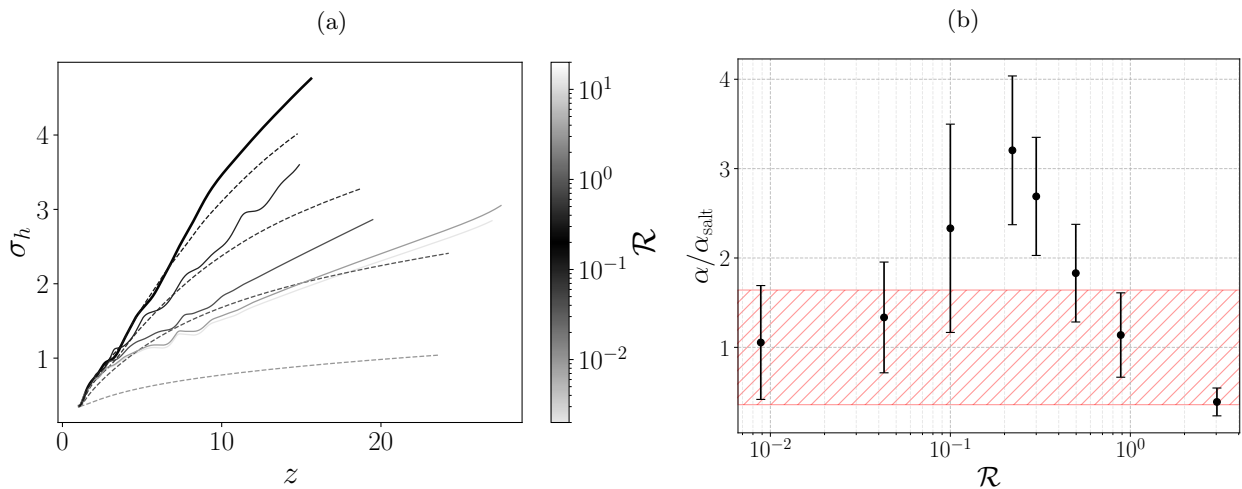


FIG. 6: (a) Evolution of the clouds' radius  $\sigma_h$  along depth. Lines are dashed if  $\mathcal{R} > 0.221$  and solid otherwise. (b) Growth rate  $\alpha$  computed in the range  $z < 0.45L_{\text{domain}}$ , divided by the reference value  $\alpha_{\text{salt}}$  of a salt-water cloud i.e. of a cloud with no particle settling ( $\mathcal{R} = 0$ ).

The clouds' growth is generally analysed along depth  $z$  rather than in time. Figure 6a shows the evolution of the radius  $\sigma_h(z)$  for all clouds. For  $\mathcal{R} \ll 1$  clouds tend to grow linearly in depth after a short transient. For  $\mathcal{R} = 0.221$  a noticeable decrease of the slope  $d\sigma_h/dz$  is visible at depth  $z = 10$ , as already observable in figure 3c, which is due to the transition to the swarm regime. For large Rouse numbers, typically above unity, it is manifest that the slope  $d\sigma_h/dz$  is never constant, it keeps decreasing as clouds fall deeper.

More importantly, figure 6a shows that the growth rate  $d\sigma_h/dz(z)$  tends to be maximum for an intermediate Rouse number close to  $\mathcal{R} = 0.221$ . To compare this growth rate with the entrainment rate measured in our experiments over a 45cm-deep field of view, the value of  $d\sigma_h/dz(z)$  is computed in simulations, then averaged in the range  $z < 0.45L_{\text{domain}}$ . The resulting average value is denoted  $\alpha$  and results are shown in figure 6b. Consistently with our experiments (see figure 6 in [1]), we observe an asymptote towards a constant growth rate as  $\mathcal{R} \rightarrow 0$ , a local maximum for a finite

Rouse number which lies in the range  $\mathcal{R} \simeq 0.3 \pm 0.1$  determined from experiments, and a clear decrease of the growth rate as  $\mathcal{R}$  increases beyond  $\mathcal{R} = 0.3$ . The maximum amplitude of the enhancement  $\alpha(\mathcal{R} = 0.221)/\alpha_{\text{salt}} = 3.20 \pm 0.83$  is larger than the value found in experiments  $\alpha(\mathcal{R} \simeq 0.3)/\alpha_{\text{salt}} = 1.75 \pm 0.30$ . This is likely due to the difference of cloud Reynolds number between experiments ( $Re = 1183$ ) and simulations ( $Re = 454$ ). In appendix B, numerical results for clouds of Reynolds number  $Re = 1183$  yield  $\alpha(\mathcal{R} = 0.221)/\alpha_{\text{salt}} = 2.20 \pm 0.42$  as a new maximum, which is in agreement with our experiments. The important point here is that the present Eulerian approach is capable of reproducing the physical effect we observed in laboratory experiments.

We now turn to the swarm regime before analysing the role of the gravitational drift in enhancing the growth rate  $\alpha$  in Section V.

### C. Swarm regime

During the gradual transition from the buoyant vortex ring to the swarm regime, particles increasingly decouple from fluid motions. This gradual decoupling is analysed thanks to the concentration  $\mathcal{C}_{\text{tracer}}$  of the passive tracer, which is implemented in four new simulations of Rouse numbers  $\mathcal{R} = 0.100, 0.221, 0.498, 0.885$ . As a wish to perform similar processings as in our experiments where the flow was visualised in a vertical laser sheet, the decoupling is illustrated with space-time diagrams in figures 7a-7d after averaging the fields  $\mathcal{C}$  and  $\mathcal{C}_{\text{tracer}}$  along  $x$  in the plane  $y = 0$  (this averaging process is made explicit with the brackets  $\langle \cdot \rangle_x$ ). The space-time diagrams reveal that increasing  $\mathcal{R}$  leads to a faster separation between the field  $\langle \mathcal{C} \rangle_x$  (in blue-red colours) and the passive tracer  $\langle \mathcal{C}_{\text{tracer}} \rangle_x$  (in yellow-red contours) which is left behind particles. By construction, the sole ingredient responsible for this decoupling is the gravitational drift in equation (9) which only concerns the field  $\mathcal{C}$ , not the passive tracer.

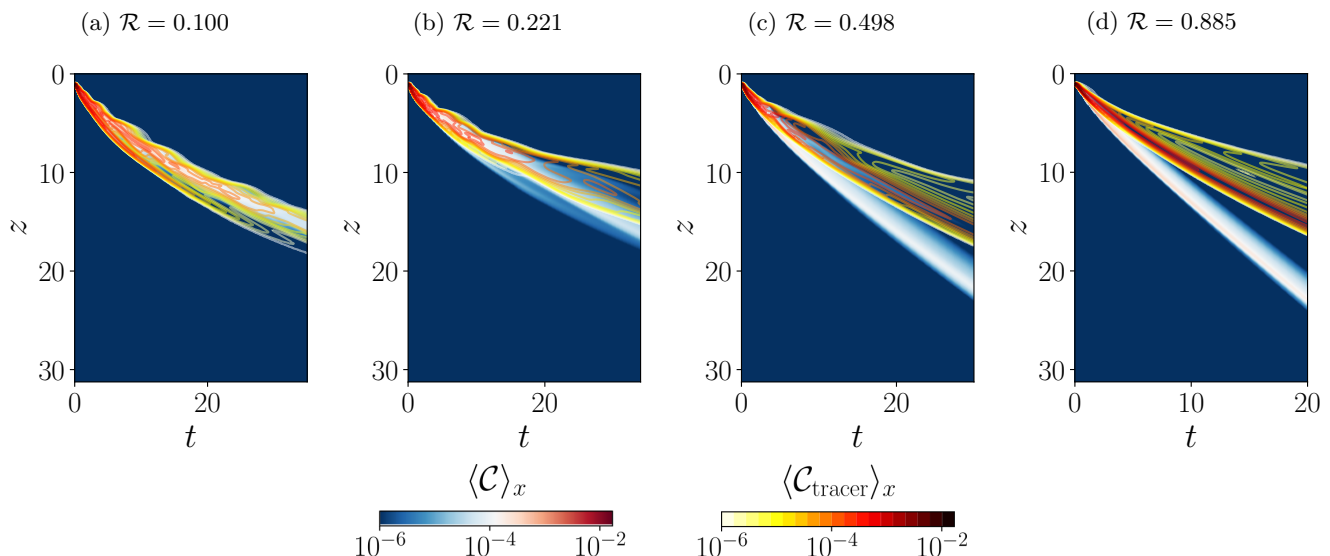


FIG. 7: Hovmöller diagrams for four increasing Rouse numbers showing the gradual decoupling in the plane  $y = 0$  between the field of concentration  $\langle \mathcal{C} \rangle_x$  (in blue-red colours) and the passive tracer  $\langle \mathcal{C}_{\text{tracer}} \rangle_x$  (in yellow-red contours).

The values shown for both concentrations are horizontal averages along  $x$  in the plane  $y = 0$  at each time step.

A quantification of the decoupling between  $\mathcal{C}$  and  $\mathcal{C}_{\text{tracer}}$  is possible by defining a correlation coefficient which computes the overlap between  $\mathcal{C}$  and  $\mathcal{C}_{\text{tracer}}$  as a percentage of the total region occupied by these two fields. In practice, minimum thresholds are applied on the fields, whose values ensure the convergence of the correlation coefficient. As in figure 7, the correlation coefficient is computed in the plane  $y = 0$  (denoted  $Oxz$  below) as

$$C_{\mathcal{C}, \mathcal{C}_{\text{tracer}}}(t) = \frac{\int_{Oxz} \xi_1(t) dx dz}{\int_{Oxz} \xi_2(t) dx dz}, \quad (14)$$

where the booleans  $(\xi_1(t), \xi_2(t))$  are defined as

$$\xi_1(t) = \begin{cases} 1, & \text{if } \mathcal{C}(t) > \mathcal{C}_1(t) \text{ and } \mathcal{C}_{\text{tracer}}(t) > \mathcal{C}_2(t) \\ 0, & \text{otherwise} \end{cases}; \quad \xi_2(t) = \begin{cases} 1, & \text{if } \mathcal{C}(t) > \mathcal{C}_1(t) \text{ or } \mathcal{C}_{\text{tracer}}(t) > \mathcal{C}_2(t) \\ 0, & \text{otherwise} \end{cases}, \quad (15)$$

with  $C_1(t) = \max\{C(t)\} \times 10^{-4}$ ,  $C_2(t) = \max\{C_{\text{tracer}}(t)\} \times 10^{-4}$ . The time evolution of  $C_{C, C_{\text{tracer}}}(t)$  is shown in figure 8a for the same four simulations as above. The correlation coefficient is initially equal to unity because both fields of concentration are identical. Then, the correlation coefficient decreases as particles gradually shift away from the passive tracer due to the gravitational drift, all the faster as the Rouse number is larger. Finally figure 8b confirms that the settling velocity of swarms approaches a constant value after separation, equal to the individual settling velocity which is equal to the Rouse number  $\mathcal{R}$  in our dimensionless units (see inlet in figure 8b). Figure 6a already showed that the growth rate of swarms starts reducing after separation (the concave deflection of  $\sigma_h(z)$  is most visible for  $\mathcal{R} = 0.221$ ), so swarms ultimately fall with constant velocity, retaining a bowl shape without deforming, as shown by the snapshots in figure 3e for  $\mathcal{R} = 3.03$ .

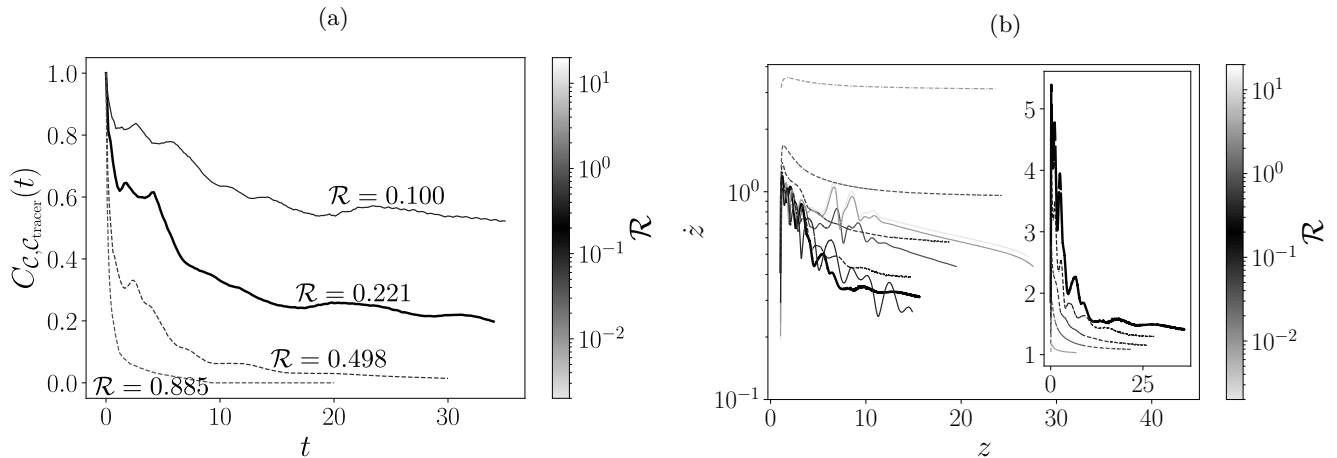


FIG. 8: (a) Time evolution of the correlation coefficient  $C_{C, C_{\text{tracer}}}(t)$  between particle and passive tracer concentrations for  $\mathcal{R} \in \{0.100, 0.221, 0.498, 0.885\}$ , from top to bottom. (b) Evolution in depth of the vertical velocity of the clouds' centre of mass for all simulations. Lines are dashed if  $\mathcal{R} > 0.221$  and solid otherwise. The inset shows the normalised velocity  $\dot{z}/\mathcal{R}$  as a function of time  $t$  only for clouds verifying  $\mathcal{R} \geq 0.221$ .

## V. ROLE OF THE ROUSE NUMBER ON THE ENHANCED GROWTH RATE

The linear growth in depth of buoyant clouds is usually described as resulting from entrainment of ambient fluid into the cloud, leading to its growth and dilution, and consequently its deceleration through mixing drag. One reference to describe the process of entrainment for turbulent thermals is the model of Morton *et al.* [2]. It is based on the entrainment hypothesis which states that the inflow velocity at the interface of the turbulent thermal is proportional to the vertical velocity of the cloud's centre of mass; this inflow velocity is considered to be produced by turbulent motions.

Yet, our observation of a maximum growth rate  $\alpha$  even for moderate Reynolds numbers ( $Re = 454$  here) suggests that the enhanced entrainment due to the finite gravitational drift finds an origin in the large-scale buoyancy-induced mean flow (which, in the case of turbulent particle clouds, is obtained by an average over realisations) rather than in turbulent fluctuations. Actually, this question of the origin of entrainment in turbulent flows has long been debated: does it originate from the large-scale mean flow incorporating ambient fluid into the turbulent region through 'engulfment'? Or from small-scale fluctuations and diffusive processes which mix the ambient material in the turbulent structure close to its interface through 'nibbling'? While Mathew and Basu [73] observed that mixing in a cylindrical turbulent jet seemed to be driven by nibbling close to the jet interface, Townsend [74] showed that large-scale eddies of increasing intensity produce more energy in the turbulent wake past a cylinder and consequently favour a larger growth rate of this wake, suggesting that the mean flow drives entrainment through engulfment. Discriminating between engulfment and nibbling can be complex because large and small scales may be insufficiently separated at moderate Reynolds numbers, and because fluxes at both scales can be connected through some relationships [73]. For example, in [75], Reynolds stresses at the mixing interface of a gravity current are modelled based on Prandtl mixing length theory, thus enabling, through the use of a large-scale quantity based on the mean flow, the description of entrainment in the mixing layer by fundamentally local fluxes.

Importantly, the reason for this ambiguity is that both processes contribute to entrainment, as evidenced by Fox [76] who derived the equations of evolution of a self-similar plume while considering the equation of conservation of energy, hence lifting the constraint of modelling entrainment to guarantee a closure of the equations. In doing so, he showed that entrainment depends both on the Reynolds stress and on a contribution from the mean flow due to buoyancy. This was confirmed by Reeuwijk and Craske [77] who carried this analysis further and showed that a third contribution comes from possible deviations from self-similarity in the streamwise direction. By analysing data from the literature, Reeuwijk and Craske [77] showed that the term of turbulence production due to shear hardly varies between a pure jet and a pure plume, even though plumes have a larger growth rate than jets. Hence this last difference between jets and plumes is attributed to the contribution of the mean flow due to buoyancy, as later confirmed by Reeuwijk *et al.* [78] in DNS. These conclusions about entrainment apply similarly for plumes and thermals, as pointed out by Landeau *et al.* [63]. From the model of Morton *et al.* [2], Landeau *et al.* [63] proved experimentally that the growth rate of an immiscible thermal verifies a linear relationship with respect to the thermal's Richardson number, which is exactly analogous to the entrainment model of Priestley and Ball [79] for plumes, see [77] for details. Consistently with these conclusions, Lecoanet *et al.* [60] showed that turbulence only enhances entrainment by 20% between turbulent thermals of Reynolds number 630 and 6300, whereas an artificial sudden shut off of buoyancy during the same numerical simulations drastically reduces the entrainment rate of turbulent thermals [61], highlighting the driving role of buoyancy in entrainment.

Consequently, in the present section we focus on mean flow azimuthally-averaged quantities to try and understand the optimum growth rate of particle clouds for a Rouse number around  $\mathcal{R} \simeq 0.22$ . Past studies have shown that in the absence of buoyancy, the circulation of a vortex ring generated from a nozzle increases from zero to a constant value during the transient rolling-up of the viscous boundary layer in the nozzle [72], with this constant circulation increasing as the ratio of the nozzle length over its diameter increases. When the vortex ring is buoyant, buoyancy provides a new contribution to the total circulation, which was fully derived by Mc Kim *et al.* [61] for a thin-cored Boussinesq vortex ring, yielding the following scaling for the growth rate  $\alpha$  (see [58, 71] but also [60, 62, 70] for turbulent thermals)

$$\alpha \propto \frac{m_0 g}{\rho_f \Gamma_\infty^2}, \quad (16)$$

with a proportionality constant accounting for the cloud added mass and its morphology [61], and with  $\Gamma_\infty$  the asymptotically constant value of the circulation. The key result here is that since all clouds undergo the same buoyancy force  $m_0 g$  in our simulations, their growth rate  $\alpha$  is dictated by  $\Gamma_\infty$  only. Consequently, vortex rings of lower circulation should have a larger growth rate – crudely speaking, they should entrain more, as consistently observed in [58, 63].

To verify this scaling, the vortex ring circulation is computed *a posteriori* for several snapshots after (i) interpolating the mesh on a regular cartesian grid, (ii) averaging the azimuthal vorticity  $\omega_\theta$  along the azimuth  $e_\theta$  in radial and vertical bins (when ambiguity is possible, we denote azimuthally-averaged quantities with an overline such as  $\overline{\omega_\theta}$ ), (iii) integrating the resulting average azimuthal vorticity over the whole radial extent and in the range  $z \in [0.3, L_{\text{domain}} - 0.3]$  (top and bottom walls are removed from this range to avoid integration of vorticity near those boundaries). Results are shown in figure 9a. We verify that the circulation produced by the particle clouds ultimately reaches a plateau, except when  $\mathcal{R} \gg 1$  i.e. for clouds which are not expected to behave as buoyant vortex rings due to separation. From previous sections, figure 9a already suggests that the circulation  $\Gamma_\infty$  is all the lower as the cloud grows faster; this is confirmed in figure 9b where the scaling  $\alpha \propto \Gamma^{-2}$  of equation (16) is in excellent agreement with the best fit (see the solid dark line in figure 9b) of measurements of the circulation when the cloud centre of mass is at mid-depth in the computational domain i.e. with the definition  $\Gamma_\infty \equiv \Gamma(z = L_{\text{domain}}/2)$ .

Another remarkable observation is the modification of the structure of the vortical core with increasing the Rouse number, as illustrated in figure 10. When  $\mathcal{R} = 4.28 \times 10^{-2}$  (figure 10a) the vortex core is neatly defined, centered around a maximum of azimuthal vorticity whose structure is at first order isotropic in a plane ( $e_r, e_z$ ) of fixed azimuth. Conversely when  $\mathcal{R} = 0.221$  (figure 10c), the vortex core is made up of sheets of vorticity of alternate sign and varying intensity which occupy a much larger region than observed for  $\mathcal{R} = 4.28 \times 10^{-2}$  at the same depth. Let us show that as  $\mathcal{R}$  gets closer to 0.221 the vortical core induces circulation farther and farther away, thus expanding the region of entrainment through the toroidal mean flow. After defining the core centroid as the barycentre of the azimuthal vorticity, the following normalised circulation is computed

$$\Gamma^*(r) = \frac{1}{\pi r^2} \int_0^{2\pi} \int_0^r \langle \omega_\theta \rangle_\theta r' dr' d\theta, \quad (17)$$

where  $(r', r, \theta)$  here correspond to polar coordinates centered on the circulation centroid. The size of the vortex core is defined as  $\text{argmax}\{\Gamma^*(r)\}$  i.e. as the radial distance from the circulation centroid where the circulation  $\Gamma^*(r)$  is

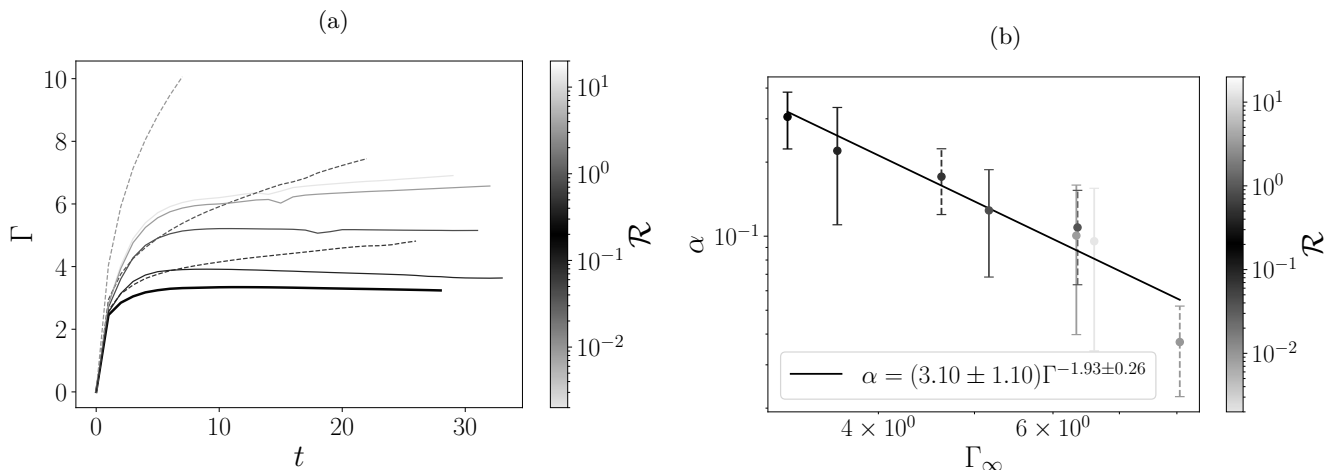


FIG. 9: (a) Time evolution of the axisymmetric circulation in the whole computational domain. Lines are dashed if  $\mathcal{R} > 0.221$  and solid otherwise. (b) Correlation between the growth rate  $\alpha$  averaged over the range  $z < 0.45$ , and measurements of  $\Gamma_\infty$ . The solid dark line is the linear least square fit of  $\ln(\alpha)$  vs.  $\ln(\Gamma_\infty)$ .

maximum. Consistently, figure 11a shows that this circulation  $\Gamma^*$  spreads further away from the circulation centroid when  $\mathcal{R} = 0.221$ , meaning that this vortex ring induces velocity farther away, therefore incorporating more ambient fluid within the particle cloud, hence the latter grows faster. This trend is even clearer in figure 11b where the core size is computed at the same depth  $L_{\text{domain}}/2$  for all clouds: one verifies that the core extension is maximum when the Rouse number is closest to  $\mathcal{R} = 0.221$ .

The key question is then: How come vortex rings have a wider core and a lower circulation when the particle Rouse number is closer to 0.221? The vortex circulation is only produced during a short initial transient, mainly by the baroclinic torque as long as its contribution along the vortex centreline is non-negligible. As soon as the buoyant material has spun up and widened sufficiently, one can define a closed contour encircling the core where no vorticity diffuses and no buoyant material is present, so that circulation is conserved (e.g. [61]). The vorticity equation along the azimuth  $e_\theta$  reads

$$\frac{D\omega_\theta}{Dt} = \underbrace{\frac{\omega_\theta v_r}{r}}_{\text{stretching}} + \overbrace{\frac{g'}{\rho_f} \frac{\partial \mathcal{C}}{\partial r}}^{\text{baroclinic torque}} + \underbrace{\nu \left[ \frac{1}{r} \frac{\partial}{\partial r} \left( r \frac{\partial \omega_\theta}{\partial r} \right) + \frac{\partial^2 \omega_\theta}{\partial z^2} \right]}_{\text{diffusion}}, \quad (18)$$

which shows that azimuthal vorticity is produced by vortex stretching, the baroclinic torque and diffusion of vorticity. The quantity  $\omega_\theta v_r$  is at first order symmetrical around the vortex core, so for a thin-cored vortex ring having a radius much larger than the vortex core, the stretching term should be vanishingly small, as previously argued by other authors [61]. Then, if diffusion is assumed negligible, most forcing is expected to originate from the baroclinic torque. This is especially true at initial times when the stretching and diffusion terms vanish while the baroclinic torque remains finite. The baroclinic torque is therefore the leading source of circulation at initial times [61]. To verify this, the dimensionless baroclinic torque  $Ri\partial_r\mathcal{C}$  along  $e_\theta$  is first averaged along the azimuth (the resulting axisymmetric torque is denoted  $\overline{Ri\partial_r\mathcal{C}}$ ). Then the axisymmetric torque is integrated in the plane ( $e_r, e_z$ ) and integrated in time until  $t = 10$  when we observe that the torque has vanished for all simulations. Results are shown in figure 12. We verify that Rouse numbers close to  $\mathcal{R} = 0.221$ , which correspond to the largest growth rate  $\alpha$  (figure 6b) and lowest circulation (figure 9a), also correspond to the lowest baroclinic forcing. This observation is robust: integrating the baroclinic torque in time even just up to  $t = 1$  modifies the value of the integrated torque, but leaves the curve in figure 12 unchanged. As an indication, the errorbars in figure 12 show the little influence of integrating the baroclinic torque up to  $t = 8$  or  $t = 10$  which respectively correspond to the lower and upper bound of errorbars.

The picture that emerges from these results is the following: under the assumption that baroclinicity is the leading forcing of the vortex rings' circulation, the maximum of entrainment capacity of particle clouds with a Rouse number close to  $\mathcal{R} = 0.221$  seems to be due to the gravitational drift and two-way coupling of particles with the fluid which

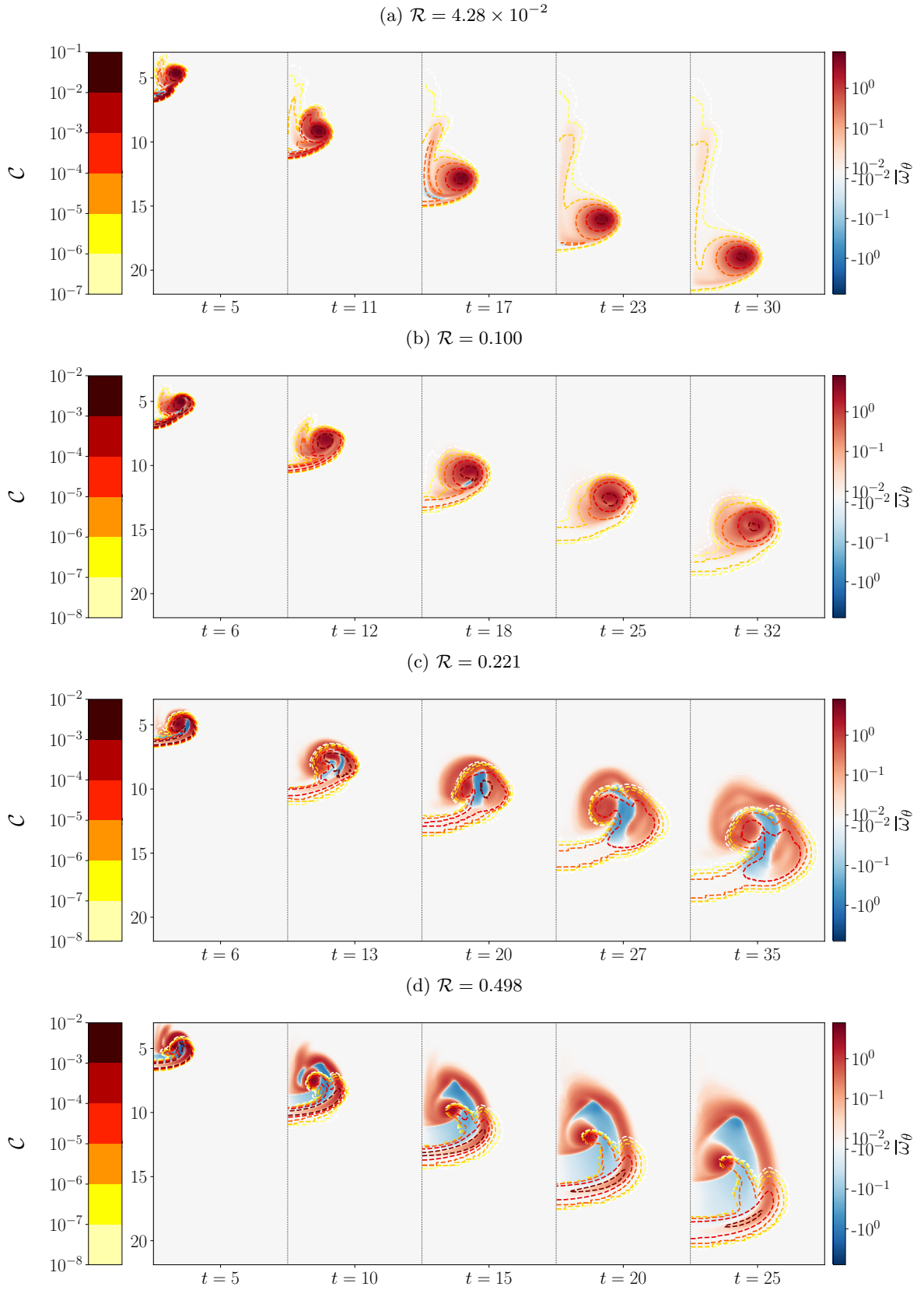


FIG. 10: Each row shows snapshots of the azimuthally-averaged vorticity  $\bar{\omega}_\theta$  in blue-red colours, and the azimuthally-averaged concentration  $\mathcal{C}$  with dashed contours in yellow-red shades (see colorbars on the left-hand side). Each snapshot is visualised in the plane  $(r, z)$  in the range  $3 < z < 22$  and  $0 < r = \sqrt{x^2 + y^2} < 10$ .

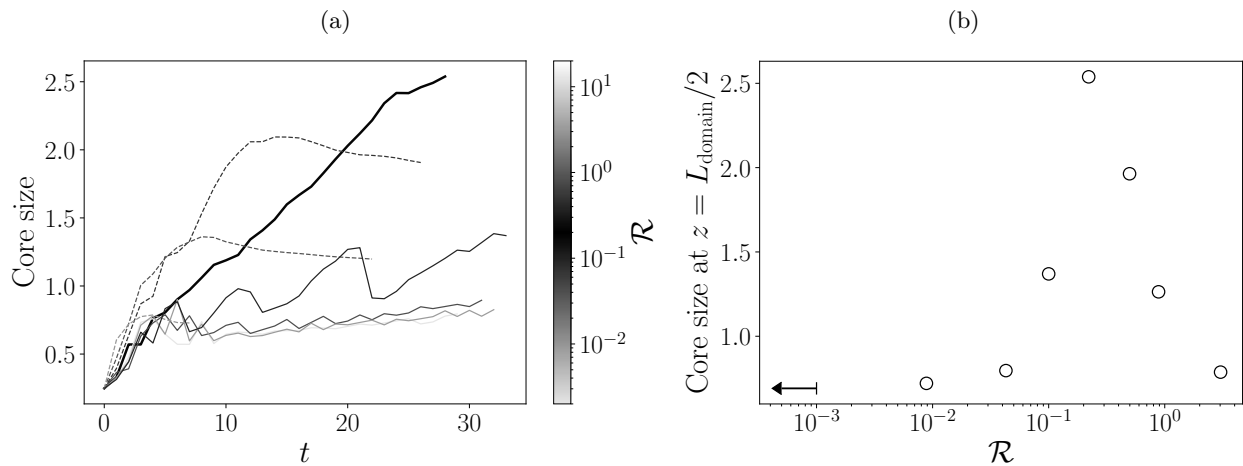


FIG. 11: (a) Time evolution of the size of the vortical core for all clouds. Lines are dashed if  $\mathcal{R} > 0.221$  and solid otherwise. (b) Size of the core at depth  $z = L_{\text{domain}}/2$  for all clouds. The dark arrow corresponds to the value for  $\mathcal{R} = 0$ .

reduces the baroclinic torque, thus reducing the cloud circulation. Since all clouds undergo an identical buoyancy force  $m_0 g$ , these same clouds have a larger growth rate  $\alpha$  as predicted by equation (16). Similar results have been obtained at a larger Reynolds number  $Re = 1183$  (see Appendix B), in good agreement with experiments. Note however that the role played by fluctuations in the limit of very large Reynolds numbers remains to be explored and might have an influence on our conclusions derived from moderate Reynolds numbers only.

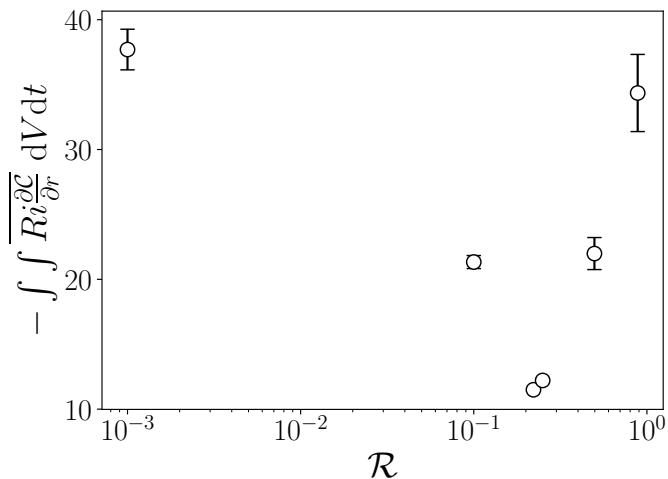


FIG. 12: Results of time and volume integration up until  $t = 10$  of the axisymmetric baroclinic torque as a function of the Rouse number.

## VI. CONCLUDING DISCUSSION

The previous section showed that the gravitational drift modifies the distribution in space and time of the field of particle concentration  $\mathcal{C}(x, y, z, t)$  compared to that of a passive tracer. This modification alters the forcing by the drag force, minimises the baroclinic torque and concurs to a maximum growth rate  $\alpha$  for a Rouse number around  $\mathcal{R} = 0.221$ . All these modifications are observed at moderate Reynolds numbers and notably quantified by the azimuthally-averaged circulation and baroclinic torque; this is consistent with the literature pointing towards the leading role of the mean flow and buoyancy in controlling entrainment and the growth of thermals (see section V).

A key conclusion is that the present Eulerian two-way coupling numerical simulations successfully reproduce our experimental observation of a maximum growth rate  $\alpha/\alpha_{\text{salt}}$  of particle clouds for a Rouse number  $\mathcal{R} \approx 0.22$  lying within the experimental range  $\mathcal{R} \simeq 0.3 \pm 0.1$ . While results at  $Re = 454$  yield a maximum growth rate slightly above the experimental value  $\alpha(\mathcal{R} \simeq 0.3)/\alpha_{\text{salt}} = 1.75 \pm 0.30$ , results at  $Re = 1183$  lie in the experimental range within uncertainty margins. A systematic study with varying Reynolds numbers might clarify whether the mechanism identified in this paper persists in the presence of intense turbulent fluctuations.

Our results raise a new question: How does the gravitational drift of particles contribute to reducing the baroclinic forcing? Some light could be shed on this matter by analysing the properties of the flow induced by a canonical laminar vortex ring while the field of concentration drifts radially outward until separation, but the evolution of the structure of the vortex core in figure 10 suggests that the feedback of particles on the vortex ring itself probably plays a non-negligible part. Furthermore, even though the robust agreement between our experiments and the present results supports the responsibility of the mean flow in the maximisation of  $\alpha$  for a finite Rouse number, it remains to be investigated whether other physical ingredients could be at play in experiments, in particular velocity fluctuations due to turbulence at much higher Reynolds numbers than considered here.

In the present numerical simulations, fluctuations are very low compared to the mean flow due to the low Reynolds number  $Re = 454$  at the scale of the particle cloud. Our experiments, on the opposite, were characterised by a Reynolds number  $Re = 1183$ . Even though this value is too low to have a well-developed turbulent flow with a clear separation of scales between the integral cloud scale and the scale of the smallest dissipative eddies, our experimental clouds evidenced some more fluctuations than in numerical simulations. On one hand, these may modify the cloud circulation during its transient increase, hence during a limited amount of time. On the other hand, after this transient, entrainment can be increased by the term of production of turbulent kinetic energy (TKE), as shown by Reeuwijk and Craske [77] in their entrainment relations. This production term may differ for one-phase turbulent thermals vs. particle-laden turbulent thermals due to turbulence modulation by particles [5], as observed in simulations [20, 21] and experiments [19, 32]. These studies notably showed a redistribution of energy from small to large wave numbers known as ‘pivoting’, which may favour nibbling-like entrainment at small scales rather than engulfment by the mean flow. Consequently, the possible enhancement of  $\alpha$  by fluctuations in a more vigorous turbulent flow cannot be ruled out, calling for further investigation with a dedicated larger experimental setup and numerical simulations with a clear separation of scales. Answering these questions also probably requires a more advanced model such as a two-fluids approach where the particles have their own velocity field (e.g. [33, 34, 80]), or a point-force Lagrangian model (e.g. [30, 81–83]).

## VII. ACKNOWLEDGEMENTS

This work was supported by the Programme National de Planétologie (PNP) of CNRS-INSU co-funded by CNES. Centre de Calcul Intensif d’Aix-Marseille is acknowledged for granting access to its high performance computing resources. This work was granted access to the HPC resources of IDRIS under the allocation 2022-A0120407543 and 2023-A0140407543 made by GENCI.

### Appendix A: Robustness of numerical measurements

We verified that numerical measurements of key quantities are invariant with respect to three numerical parameters: (i) the Schmidt number  $Sc = \nu/\kappa_p$ , (ii) the size  $h_{\text{min}}$  of the finest mesh cell and (iii) the numerical scheme implemented to compute the concentration gradient. For all simulations presented in the core of this study, the concentration gradient was computed with the generalised minmod slope limiter [52], which reads along the direction  $\mathbf{e}_z$

$$\left(\frac{\partial \mathcal{C}}{\partial z}\right)_i \simeq \max \left\{ 0, \min \left( \theta(\mathcal{C}_{i+1} - \mathcal{C}_i), \theta(\mathcal{C}_i - \mathcal{C}_{i-1}), \frac{\mathcal{C}_{i+1} - \mathcal{C}_{i-1}}{2} \right) \right\}, \quad (\text{A1})$$

with  $\theta$  a scalar ranging between 1 (the most dissipative scheme) and 2 (the least dissipative scheme), and  $\mathcal{C}_{j \in \mathbb{N}}$  is the evaluation of  $\mathcal{C}$  in a mesh cell  $j$  along the direction  $\mathbf{e}_z$ . The default value  $\theta = 1.3$  of Basilisk was adopted. We verified that adopting a second-order centered scheme

$$\left(\frac{\partial \mathcal{C}}{\partial z}\right)_i = \frac{\mathcal{C}_{i+1} - \mathcal{C}_{i-1}}{2} \quad (\text{A2})$$

does not alter our measurements. Results are presented in table I, providing the average and standard deviation of (a) the growth rate  $\alpha$ , (b) the cloud vertical velocity  $\dot{z}$  and (c) the work of the drag term  $\int \mathcal{C}v_z$  responsible for the

Varying numerical parameter	Fixed $Re$	$\alpha \times 10^3$	$\dot{z} \times 10^2$	$\int \mathcal{C}v_z \times 10^3$
$Sc \in \{1, 2, 5, 10\}$	1183	$172 \pm 7$	$640 \pm 2$	$13.8 \pm 2.3$
$L_{\text{domain}}/h_{\text{min}} \in \{256, 512, 1024, 2048\}$	180	$328 \pm 31$	$42.9 \pm 3.4$	$6.4 \pm 1.0$
$L_{\text{domain}}/h_{\text{min}} \in \{256, 512, 1024, 2048\}$	454	$321 \pm 29$	$44.1 \pm 4.9$	$6.7 \pm 1.5$
$L_{\text{domain}}/h_{\text{min}} \in \{512, 1024, 2048\}$	1183	$343 \pm 28$	$56 \pm 14$	$12.7 \pm 7.4$
$\nabla\mathcal{C}$ : minmod2 or 2nd order centered	454	$305.64 \pm 0.03$	$38.7870 \pm 0.0004$	$5.422522 \pm 0.000006$
$\nabla\mathcal{C}$ : minmod2 or 2nd order centered	1183	$295 \pm 8$	$39.9 \pm 0.6$	$5.7 \pm 0.2$

TABLE I: Variability of the macroscopic quantities  $\alpha$ ,  $\dot{z}$  and the work of the drag force  $\int \mathcal{C}v_z$  in the range  $z < 0.45L_{\text{domain}}$  when varying the Schmidt number, the size  $h_{\text{min}}$  of the finest mesh cell, or the numerical scheme used to compute the concentration gradient.

transfer of energy from particles to the fluid during the cloud fall. These three quantities are averaged when the cloud position verifies  $z(t) < 0.45L_{\text{domain}}$ , which is the range we analysed with our experiments [1]. Reported values evidence little to negligible impact of the three numerical parameters on average measurements of  $\alpha$ ,  $\dot{z}$  and  $\int \mathcal{C}v_z$ .

### Appendix B: Key results for clouds of Reynolds number $Re = 1183$

For completeness, we briefly present numerical results for clouds of Reynolds number  $Re = 1183$  as in our experiments [1]. Figure 13 shows time averages in the plane  $y = 0$  of the field of concentration  $\mathcal{C}$  for a set of clouds with varying Rouse numbers. More fluctuations do appear at low Rouse numbers (figures 13a-13c), whereas clouds of large Rouse numbers still evidence a thin bowl shape due to rapid particle separation from fluid motions (figures 13d,13e). Importantly, these images show the existence of a maximum growth rate as  $\mathcal{R} \rightarrow 0.221$ , as quantitatively confirmed by figure 14, similarly as in section IV B and consistently with our experiments [1]. The maximum amplitude of the enhancement  $\alpha(\mathcal{R} = 0.221)/\alpha_{\text{salt}} = 2.20 \pm 0.42$  is lower than the one measured for  $Re = 454$  in section IV B, and in good agreement with the maximum measured in experiments  $\alpha(\mathcal{R} \simeq 0.3)/\alpha_{\text{salt}} = 1.75 \pm 0.30$ . A systematic study as a function of the Reynolds number might clarify what determines the amplitude of the optimum  $\alpha/\alpha_{\text{salt}}$ , but this is beyond the scope of the present work which focuses on the origin of this amplification, and on the capacity of the numerical model to reproduce it.

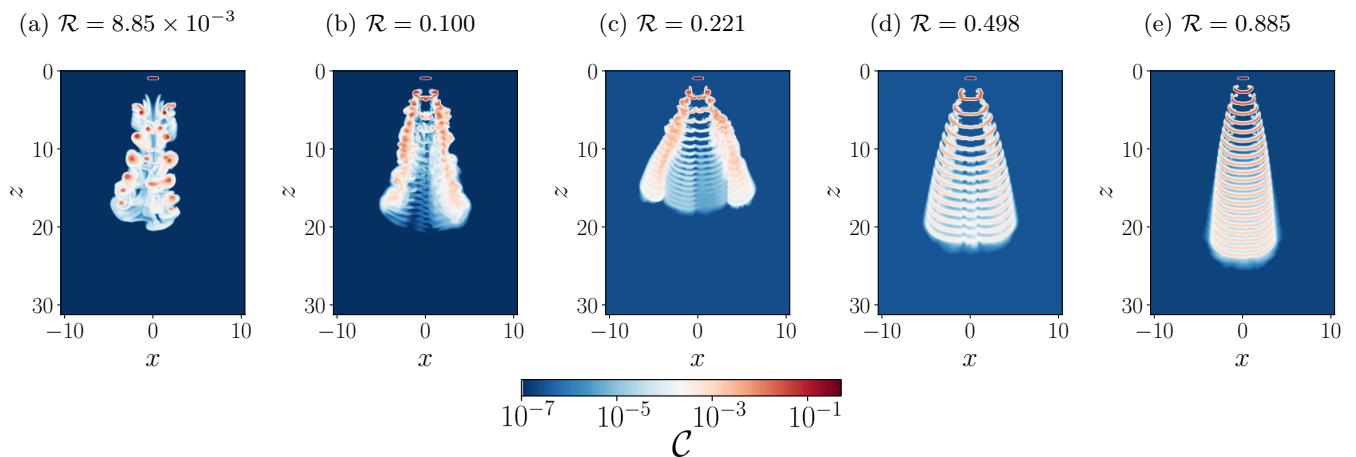


FIG. 13: Field of concentration  $\mathcal{C}$  in the plane  $y = 0$  averaged over up to 20 snapshots taken with a constant timestep  $\Delta t = 2.5$  over the cloud fall for clouds of Reynolds number  $Re = 1183$ .

- 
- [1] Q. Kriaa, E. Subra, B. Favier, and M. Le Bars, Effects of particle size and background rotation on the settling of particle clouds, *Physical Review Fluids* **7**, 124302 (2022).  
[2] B. R. Morton, G. I. Taylor, and J. S. Turner, Turbulent gravitational convection from maintained and instantaneous sources, *Proceedings of the Royal Society of London. Series A. Mathematical and Physical Sciences* **234**, 1 (1956).

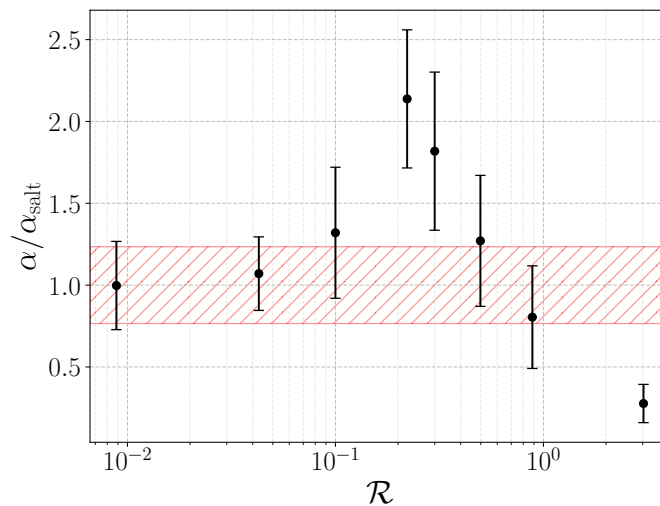


FIG. 14: Growth rate  $\alpha$  computed in the range  $z < 0.45L_{\text{domain}}$ , divided by the reference value  $\alpha_{\text{salt}}$  of a salt-water cloud i.e. of a cloud with no particle settling ( $\mathcal{R} = 0$ ). The Reynolds number is  $Re = 1183$ .

- [3] T. Rückriemen, D. Breuer, and T. Spohn, The Fe snow regime in Ganymede’s core: A deep-seated dynamo below a stable snow zone, *Journal of Geophysical Research: Planets* **120**, 1095 (2015).
- [4] S. Balachandar and J. K. Eaton, Turbulent Dispersed Multiphase Flow, *Annual Review of Fluid Mechanics* **42**, 111 (2010).
- [5] L. Brandt and F. Coletti, Particle-Laden Turbulence: Progress and Perspectives, *Annual Review of Fluid Mechanics* **54**, 159 (2022).
- [6] G. H. Good, P. J. Ireland, G. P. Bewley, E. Bodenschatz, L. R. Collins, and Z. Warhaft, Settling regimes of inertial particles in isotropic turbulence, *Journal of Fluid Mechanics* **759** (2014).
- [7] H. Yoshimoto and S. Goto, Self-similar clustering of inertial particles in homogeneous turbulence, *Journal of Fluid Mechanics* **577**, 275 (2007).
- [8] S. Goto and J. C. Vassilicos, Sweep-Stick Mechanism of Heavy Particle Clustering in Fluid Turbulence, *Physical Review Letters* **100**, 054503 (2008).
- [9] F. Falkinoff, M. Obligado, M. Bourgoïn, and P. D. Mininni, Preferential Concentration of Free-Falling Heavy Particles in Turbulence, *Physical Review Letters* **125**, 064504 (2020).
- [10] M. R. Maxey, The gravitational settling of aerosol particles in homogeneous turbulence and random flow fields, *Journal of Fluid Mechanics* **174**, 441 (1987).
- [11] S. Ghosh, J. Dávila, J. Hunt, A. Srdic, H. Fernando, and P. Jonas, How turbulence enhances coalescence of settling particles with applications to rain in clouds, *Proceedings of the Royal Society A: Mathematical, Physical and Engineering Sciences* **461**, 3059 (2005).
- [12] A. Aliseda, A. Cartellier, F. Hainaux, and J. C. Lasheras, Effect of preferential concentration on the settling velocity of heavy particles in homogeneous isotropic turbulence, *Journal of Fluid Mechanics* **468**, 77 (2002).
- [13] J. P. L. C. Salazar, J. D. Jong, L. Cao, S. H. Woodward, H. Meng, and L. R. Collins, Experimental and numerical investigation of inertial particle clustering in isotropic turbulence, *Journal of Fluid Mechanics* **600**, 245 (2008).
- [14] F. Toschi and E. Bodenschatz, Lagrangian Properties of Particles in Turbulence, *Annual Review of Fluid Mechanics* **41**, 375 (2009).
- [15] J. Bec, L. Biferale, G. Boffetta, A. Celani, M. Cencini, A. Lanotte, S. Musacchio, and F. Toschi, Acceleration statistics of heavy particles in turbulence, *Journal of Fluid Mechanics* **550**, 349 (2006).
- [16] L.-P. Wang and M. R. Maxey, Settling velocity and concentration distribution of heavy particles in homogeneous isotropic turbulence, *Journal of Fluid Mechanics* **256**, 27 (1993).
- [17] P. Nielsen, Turbulence effects on the settling of suspended particles, *Journal of Sedimentary Research* **63**, 835 (1993).
- [18] M. R. Maxey and S. Corrsin, Gravitational Settling of Aerosol Particles in Randomly Oriented Cellular Flow Fields, *Journal of the Atmospheric Sciences* **43**, 1112 (1986).
- [19] R. Hassaini and F. Coletti, Scale-to-scale turbulence modification by small settling particles, *Journal of Fluid Mechanics* **949**, A30 (2022).
- [20] S. Elghobashi and G. C. Truesdell, On the two-way interaction between homogeneous turbulence and dispersed solid particles. I: Turbulence modification, *Physics of Fluids A: Fluid Dynamics* **5**, 1790 (1993).
- [21] T. Bosse, L. Kleiser, and E. Meiburg, Small particles in homogeneous turbulence: Settling velocity enhancement by two-way coupling, *Physics of Fluids* **18**, 027102 (2006).
- [22] R. Monchaux and A. Dejoan, Settling velocity and preferential concentration of heavy particles under two-way coupling effects in homogeneous turbulence, *Physical Review Fluids* **2**, 104302 (2017).

- [23] E. Kruger, *Dynamics of Downdraughts and Cold Pools: An Experimental and Numerical Study*, Thesis, University of Cambridge (2020).
- [24] R. Ouillon, E. Meiburg, and B. R. Sutherland, Turbidity currents propagating down a slope into a stratified saline ambient fluid, *Environmental Fluid Mechanics* **19**, 1143 (2019).
- [25] F. Necker, C. Härtel, L. Kleiser, and E. Meiburg, High-resolution simulations of particle-driven gravity currents, *International Journal of Multiphase Flow* **28**, 279 (2002).
- [26] A. Fabregat Tomàs, A. C. Poje, T. M. Özgökmen, and W. K. Dewar, Numerical simulations of rotating bubble plumes in stratified environments, *Journal of Geophysical Research: Oceans* **122**, 6795 (2017).
- [27] G. Boffetta, A. Celani, F. D. Lillo, and S. Musacchio, The Eulerian description of dilute collisionless suspension, *Europhysics Letters* **78**, 14001 (2007).
- [28] J. F. Reali, P. Garaud, A. Alsinan, and E. Meiburg, Layer formation in sedimentary fingering convection, *Journal of Fluid Mechanics* **816**, 268 (2017).
- [29] J. Lemus, A. Fries, P. A. Jarvis, C. Bonadonna, B. Chopard, and J. Lätt, Modelling Settling-Driven Gravitational Instabilities at the Base of Volcanic Clouds Using the Lattice Boltzmann Method, *Frontiers in Earth Science* **9** (2021).
- [30] Y.-J. Chou and Y.-C. Shao, Numerical study of particle-induced Rayleigh-Taylor instability: Effects of particle settling and entrainment, *Physics of Fluids* **28**, 043302 (2016).
- [31] M. R. Maxey and J. J. Riley, Equation of motion for a small rigid sphere in a nonuniform flow, *The Physics of Fluids* **26**, 883 (1983).
- [32] T. Berk and F. Coletti, Dynamics of small heavy particles in homogeneous turbulence: A Lagrangian experimental study, *Journal of Fluid Mechanics* **917**, A47 (2021).
- [33] S. Nasab and P. Garaud, Preferential concentration by mechanically driven turbulence in the two-fluid formalism, *Physical Review Fluids* **6**, 104303 (2021).
- [34] M. Magnani, S. Musacchio, and G. Boffetta, Inertial effects in dusty Rayleigh–Taylor turbulence, *Journal of Fluid Mechanics* **926** (2021).
- [35] C. T. Jacobs, T. J. Goldin, G. S. Collins, M. D. Piggott, S. C. Kramer, H. J. Melosh, C. R. G. Wilson, and P. A. Allison, An improved quantitative measure of the tendency for volcanic ash plumes to form in water: Implications for the deposition of marine ash beds, *Journal of Volcanology and Geothermal Research* **290**, 114 (2015).
- [36] É. Guazzelli and J. F. Morris, *A Physical Introduction to Suspension Dynamics*, Cambridge Texts in Applied Mathematics (Cambridge University Press, Cambridge, 2011).
- [37] G. Subramanian and D. L. Koch, Evolution of clusters of sedimenting low-Reynolds-number particles with Oseen interactions, *Journal of Fluid Mechanics* **603**, 63 (2008).
- [38] F. Pignatelli, M. Nicolas, and É. Guazzelli, A falling cloud of particles at a small but finite Reynolds number, *Journal of Fluid Mechanics* **671**, 34 (2011).
- [39] W. B. Daniel, R. E. Ecke, G. Subramanian, and D. L. Koch, Clusters of sedimenting high-Reynolds-number particles, *Journal of Fluid Mechanics* **625**, 371 (2009).
- [40] D. L. Koch, Hydrodynamic diffusion in a suspension of sedimenting point particles with periodic boundary conditions, *Physics of Fluids* **6**, 2894 (1994).
- [41] A. J. C. Ladd, Dynamical simulations of sedimenting spheres, *Physics of Fluids A: Fluid Dynamics* **5**, 299 (1993).
- [42] J. M. Ham and G. M. Homsy, Hindered settling and hydrodynamic dispersion in quiescent sedimenting suspensions, *International Journal of Multiphase Flow* **14**, 533 (1988).
- [43] H. Nicolai and E. Guazzelli, Effect of the vessel size on the hydrodynamic diffusion of sedimenting spheres, *Physics of Fluids* **7**, 3 (1995).
- [44] J. Martin, N. Rakotomalala, and D. Salin, Hydrodynamic dispersion broadening of a sedimentation front, *Physics of Fluids* **6**, 3215 (1994).
- [45] J.-Z. Xue, E. Herbolzheimer, M. A. Rutgers, W. B. Russel, and P. M. Chaikin, Diffusion, dispersion, and settling of hard spheres, *Physical Review Letters* **69**, 1715 (1992).
- [46] S. Lee, Y. Jang, C. Choi, and T. Lee, Combined effect of sedimentation velocity fluctuation and self-sharpening on interface broadening, *Physics of Fluids A: Fluid Dynamics* **4**, 2601 (1992).
- [47] R. H. Davis, Hydrodynamic diffusion of suspended particles: A symposium, *Journal of Fluid Mechanics* **310**, 325 (1996).
- [48] É. Guazzelli and J. Hinch, Fluctuations and Instability in Sedimentation, *Annual Review of Fluid Mechanics* **43**, 97 (2011).
- [49] S. Elghobashi, On predicting particle-laden turbulent flows, *Applied Scientific Research* **52**, 309 (1994).
- [50] S. Popinet, An accurate adaptive solver for surface-tension-driven interfacial flows, *Journal of Computational Physics* **228**, 5838 (2009).
- [51] J. B. Bell, P. Colella, and H. M. Glaz, A second-order projection method for the incompressible navier-stokes equations, *Journal of Computational Physics* **85**, 257 (1989).
- [52] Basilisk - src/utls.h, <http://basilisk.fr/src/utls.h>.
- [53] H. Rahimipour and D. Wilkinson, Dynamic behaviour of particle clouds, in *11th Australasian Fluid Mechanics Conference University of Tasmania, Hobart, Australia* (1992).
- [54] J. W. M. Bush, B. A. Thurber, and F. Blanchette, Particle clouds in homogeneous and stratified environments, *Journal of Fluid Mechanics* **489**, 29 (2003).
- [55] A. C. H. Lai, R.-Q. Wang, A. W.-K. Law, and E. E. Adams, Modeling and experiments of polydisperse particle clouds, *Environmental Fluid Mechanics* **16**, 875 (2016).
- [56] T. S. Pottebaum and M. Gharib, The pinch-off process in a starting buoyant plume, *Experiments in Fluids* **37**, 87 (2004).

- [57] M. Gharib, E. Rambod, and K. Shariff, A universal time scale for vortex ring formation, *Journal of Fluid Mechanics* **360**, 121 (1998).
- [58] D. Bond and H. Johari, Effects of initial geometry on the development of thermals, *Experiments in Fluids* **39**, 591 (2005).
- [59] V. Lherm, *Thermal and chemical partitioning dynamics during the differentiation of terrestrial planets*, Ph.D. thesis, Université de Lyon (2021).
- [60] D. Lecoanet and N. Jeevanjee, Entrainment in Resolved, Dry Thermals, *Journal of the Atmospheric Sciences* **76**, 3785 (2019).
- [61] B. McKim, N. Jeevanjee, and D. Lecoanet, Buoyancy-driven entrainment in dry thermals, *Quarterly Journal of the Royal Meteorological Society* **146**, 415 (2020).
- [62] J. S. Turner and G. I. Taylor, Buoyant vortex rings, *Proceedings of the Royal Society of London. Series A. Mathematical and Physical Sciences* **239**, 61 (1957).
- [63] M. Landeau, R. Deguen, and P. Olson, Experiments on the fragmentation of a buoyant liquid volume in another liquid, *Journal of Fluid Mechanics* **749**, 478 (2014).
- [64] D. Bond and H. Johari, Impact of buoyancy on vortex ring development in the near field, *Experiments in Fluids* **48**, 737 (2010).
- [65] B. Zhao, A. W. K. Law, A. C. H. Lai, and E. E. Adams, On the internal vorticity and density structures of miscible thermals, *Journal of Fluid Mechanics* **722**, R5 (2013).
- [66] J. S. Turner, The ‘starting plume’ in neutral surroundings, *Journal of Fluid Mechanics* **13**, 356 (1962).
- [67] G. J. Ruggaber, Dynamics of sediment clouds related to open-water sediment disposal, PhD MIT (2000).
- [68] A. C. H. Lai, B. Zhao, A. W.-K. Law, and E. E. Adams, Two-phase modeling of sediment clouds, *Environmental Fluid Mechanics* **13**, 435 (2013).
- [69] M. Moghadaripour, Experimental Study of Particle Clouds in Stagnant Water, ASCE (2017).
- [70] R. S. Scorer, Experiments on convection of isolated masses of buoyant fluid, *Journal of Fluid Mechanics* **2**, 583 (1957).
- [71] V. V. Nikulin, Analytical model of motion of turbulent vortex rings in an incompressible fluid, *Journal of Applied Mechanics and Technical Physics* **55**, 558 (2014).
- [72] N. Didden, On the formation of vortex rings: Rolling-up and production of circulation, *Zeitschrift für angewandte Mathematik und Physik ZAMP* **30**, 101 (1979).
- [73] J. Mathew and A. J. Basu, Some characteristics of entrainment at a cylindrical turbulence boundary, *Physics of Fluids* **14**, 2065 (2002).
- [74] A. Townsend, LXXXI. The eddy viscosity in turbulent shear flow, *The London, Edinburgh, and Dublin Philosophical Magazine and Journal of Science* **41**, 890 (1950).
- [75] P. Odier, J. Chen, and R. E. Ecke, Understanding and modeling turbulent fluxes and entrainment in a gravity current, *Physica D: Nonlinear Phenomena Special Issue on Small Scale Turbulence*, **241**, 260 (2012).
- [76] D. G. Fox, Forced plume in a stratified fluid, *Journal of Geophysical Research (1896-1977)* **75**, 6818 (1970).
- [77] M. van Reeuwijk and J. Craske, Energy-consistent entrainment relations for jets and plumes, *Journal of Fluid Mechanics* **782**, 333 (2015).
- [78] M. van Reeuwijk, P. Salizzoni, G. R. Hunt, and J. Craske, Turbulent transport and entrainment in jets and plumes: A DNS study, *Physical Review Fluids* **1**, 074301 (2016).
- [79] C. H. B. Priestley and F. K. Ball, Continuous convection from an isolated source of heat, *Quarterly Journal of the Royal Meteorological Society* **81**, 144 (1955).
- [80] K. Nakamura, H. N. Yoshikawa, Y. Tasaka, and Y. Murai, Linear stability analysis of bubble-induced convection in a horizontal liquid layer, *Physical Review E* **102**, 053102 (2020).
- [81] Y. Yamamoto, F. Hisataka, and S. Harada, Numerical simulation of concentration interface in stratified suspension: Continuum–particle transition, *International Journal of Multiphase Flow* **73**, 71 (2015).
- [82] E. Climent and J. Magnaudet, Large-Scale Simulations of Bubble-Induced Convection in a Liquid Layer, *Physical Review Letters* **82**, 4827 (1999).
- [83] I. M. Mazzitelli and D. Lohse, Evolution of energy in flow driven by rising bubbles, *Physical Review E* **79**, 066317 (2009).